

# Energy transfer and budget analysis for transient process with operator-driven reduced-order model

Yuto Nakamura<sup>†</sup>, Yuma Kuroda, Shintaro Sato, and Naofumi Ohnishi

Department of Aerospace Engineering, Tohoku University, Sendai, 980-8579, Japan

(Received xx; revised xx; accepted xx)

We present the possibility of energy transfer and budget analysis for transient flow using eigenmodes of the operator from the Navier–Stokes equation. We derive the energy transfer equation, which provides the energy budget for the eigenmodes, through the Galerkin projection of the equation using the bi-orthogonality of the eigenmodes and the adjoint mode. Energy budget and transfer analysis between modes were conducted for two-dimensional flow around a cylinder with eigenmodes growing or decaying from a steady flow. Using the linearized energy transfer equation and eigenmodes from global stability analysis, we identify the energy budget and spatial distribution that determine growth rates of the modes. Moreover, energy budget and transfer analysis are realized by considering the time evolution of the eigenmodes, even during the nonlinear development of the eigenmodes. By introducing time-varying dynamic mode decomposition with a phase-control strategy for multiple time-series datasets from numerical simulations of the phase-controlled initial flow, time-varying eigenmodes are extracted in the transient two-dimensional cylinder flow. With the extracted time-dependent modes and the derived energy transfer equations, the time evolution of the energy budget and spatial distribution of energy transfer can be computed until the eigenmodes developed from the steady field reach the post-transient periodic flow. The temporal evolution of the energy budget and transfer distribution reveals that transient growth processes display different time-dependent characteristics of energy transfer, even in cylinder flows at Reynolds numbers that eventually lead to a periodic state.

**Key words:**

---

## 1. Introduction

Energy transfer due to the nonlinearity and viscous diffusion effects plays a fundamental role in fluid dynamics, governing phenomena such as vortex dynamics (Biswas & Buxton 2024; Freeman *et al.* 2023; Nakamura *et al.* 2025b), bifurcation instability (Noack *et al.* 2003; Deng *et al.* 2019; Mittal 2009), transient development (Zhong *et al.* 2025; Ballouz *et al.* 2024), and turbulence (Yamada & Ohkitani 1991; Nekkanti *et al.* 2025; Yeung & Schmidt 2025). Consequently, the budget of energy diffusion and transfer across different scales has been investigated through various approaches. Recent advances in data-driven science

<sup>†</sup> Email address for correspondence: yuto.nakamura.t4@dc.tohoku.ac.jp

(Taira *et al.* 2017, 2020; Schmidt 2020; Towne *et al.* 2018; Schmid 2010; Fukami 2024) have enabled the extraction of coherent structures embedded in complex fluid flows and their decomposition into different scales. Furthermore, these advancements have clarified the energy transfer mechanisms between different scales. However, for transient flows undergoing nonlinear development, even decomposing flow structures into distinct scales remains a challenge. This paper presents the decomposition of transient flow into components of different scales, characterized by their frequencies, and analyzes the energy budget, considering both viscous diffusion and energy transfer.

Several modal decomposition methods exist for extracting coherent structures that reveal energy transfer and the energy budget in fluid flow. One approach is to decompose the flow field into orthonormal modes. By projecting the governing equations onto a low-dimensional subspace spanned by these orthonormal modes, the viscous diffusion of the modes and their interactions can be studied. This approach is referred to as the Galerkin projection approach or Galerkin model (Noack & Eckelmann 1994b; Kunisch & Volkwein 2002), and the low-dimensional model is referred to as a reduced-order model (ROM). A well-known method for finding an orthonormal basis is proper orthogonal decomposition (POD) (Berkooz *et al.* 1993; Holmes 2012; Lumley 1967). POD extracts the most energetic modes from a flow dataset. Noack *et al.* (2003) demonstrated that the energy budget of each mode can be computed in a projection-based ROM using POD modes for the periodic flow around a two-dimensional cylinder. However, POD assumes a simple representation in terms of orthonormal bases, which means that a single mode may contain multiple frequency components. This limitation makes POD unsuitable for analyzing energy transfer between different frequencies.

Because of its ability to decompose into frequency-wise modes, decomposition in the spectral domain using wavelet analysis (Morlet *et al.* 1982; Goupillaud *et al.* 1984; Rinoshika & Rinoshika 2020; Ballouz *et al.* 2024) and Fourier decomposition (Freeman *et al.* 2024; Towne *et al.* 2018) are the most fundamental and widely used methods for energy transfer and budget analysis. Wavelet analysis has been used to analyze the energy budget and transfer related to high-frequency spectra in turbulent flows because of its ability to achieve high temporal resolution in the high-frequency domain (Yamada & Ohkitani 1991). In contrast, the Fourier decomposition is effective in resolving the low-frequency region. Since the low-frequency components characterize the large-scale structure of the flow fields, Fourier decomposition is used to study the energy transfer related to the primary structure.

To extract large-scale coherent structures in turbulence, spectral proper orthogonal decomposition (SPOD) (Towne *et al.* 2018; Schmidt & Colonius 2020) has been developed to identify statistically significant modes at each frequency from Fourier modes. The original POD directly extracts the modes with the largest energy from the flow field dataset. However, the extracted modes may contain structures of different frequencies, which makes them unsuitable for analyzing energy transfer between different frequencies. SPOD addresses this limitation by performing POD on a frequency-by-frequency basis, thus ensuring that each mode corresponds to a single frequency component. The introduction of SPOD has significantly advanced energy transfer analysis by enabling the efficient extraction of dominant frequency components, even in turbulent flows.

Schmidt (2020) quantified the interaction between different frequencies, which drives energy transfer, using the bispectrum and proposed bispectral mode decomposition (BMD), which extracts the mode that maximizes the bispectrum and identifies the spatial regions where the interaction is strong. BMD has been applied to numerous flow situations, such as the wake flow of a turbine blade (Biswas & Buxton 2024), cylinder flow (Nakamura *et al.*

2025b), and jet flow (Nekkanti *et al.* 2025; Yeung & Schmidt 2025). The relationship among the spatial distribution of interactions, the bispectrum, and energy transfer has been discussed.

Although the bispectrum characterizes the strength of nonlinear interaction, it does not quantify the amount of energy transfer. To address this limitation, Freeman *et al.* (2024) derived the Fourier-averaged Navier–Stokes equation (FANS), which is the Fourier decomposition of the Navier–Stokes equations, providing a way to physically interpret the bispectrum maximized by BMD. Based on FANS, the kinetic energy budget for the frequency component  $f_k$  ( $k = 1, 2, \dots$ ) is given by

$$\text{Real} \left( - \sum_{i=-\infty}^{\infty} \int \hat{\mathbf{u}}_{f_k}^H (\hat{\mathbf{u}}_{f_k-f_i} \cdot \nabla) \hat{\mathbf{u}}_{f_i} d\mathbf{x} + \frac{1}{Re} \int \hat{\mathbf{u}}_{f_k}^H \nabla^2 \hat{\mathbf{u}}_{f_k} d\mathbf{x} \right) = 0, \quad (1.1)$$

where  $\hat{\mathbf{u}}_{f_k}$  is the spectrum of the  $f_k$ -frequency component, and Real denotes the real part of a complex value. The first term represents the triadic energy transfer related to  $f_k$ ,  $f_i$ , and  $f_k - f_i$ , while the second term represents the viscous diffusion effect. Through the first term, the frequency  $f_i$  component transfers energy to the  $f_k$  component. Computing the values of these terms from the Fourier modes, i.e., the spectrum reveals the energy transfer relationship between the  $f_k$ - and  $f_i$ -components, as well as the diffusion effect on the  $f_k$ -component.

Yeung *et al.* (2024) focused on the triadic energy transfer term obtained from FANS. They proposed triadic orthogonal decomposition (TOD) to extract the spatial structure that maximizes this triadic energy transfer term. By employing TOD, the frequency components that maximize their transfer relations and the local spatial structures in which energy transfer occurs are revealed for frequencies with arbitrary triadic relations. However, none of BMD, FANS, or TOD is directly applicable to transiently developing flows, as they all rely on decomposition into Fourier modes, which assumes a statistically stationary flow without long-term growing or decaying components. Applying mode decomposition optimized for weakly stationary flows to transient flows fails to capture the short-term behavior of the transient process (Schmid 2007). Because many natural and engineering flows exhibit transient development, extending energy transfer analysis to transient flows is crucial for understanding fluid dynamics.

To handle the triadic energy transfer between different frequencies in transient processes and viscous diffusion, a modal decomposition technique is required for the transient process. To account for transient flows, Amiri-Margavi & Babaee (2024) proposed the use of optimally time-dependent (OTD) modes, computed at each time step, which explicitly incorporate the time dependence of the modal structures. By enabling the time variation of the spatial distribution during the transient process, the transiently developing flow field can be optimally decomposed. The OTD formulation is similar to extracting POD modes for a specific time in a transient process rather than decomposing it in the frequency domain. Ohmichi (2024) extended the variational mode decomposition, which can extract signals with variation in a specific frequency bandwidth, to flow fields and succeeded in decomposing transient flows into time-dependent modes with a specific center frequency.

Another approach for mode extraction is to consider the operators derived from the Navier–Stokes equations. Global stability analysis (GSA) (Noack & Eckelmann 1994a; Ohmichi 2014; Ohmichi & Yamada 2021; Ranjan *et al.* 2020) extracts global modes that can grow linearly from a base flow. To examine the eigenvalues of operators linearized around the base flow, the growth and decay of the corresponding eigenmodes, along with their frequencies, are determined. Dynamic mode decomposition (DMD) (Schmid 2010, 2022; Tu 2013) is a method that can extract eigenmodes of a discrete dataset based on a linear operator, assuming that the dataset is time-advanced by the operator. Strictly speaking, DMD is not a method to extract eigenmodes from an operator, but DMD modes are comparable

to eigenmodes of the operator. However, these methods are specialized for dealing with linear growth or decay from base flow. They are not suitable for direct application to transient processes because linear operators around a particular base flow cannot describe the nonlinear time evolution associated with variations in the base flow.

To decompose a transient process into eigenmodes of an operator, one approach is to consider the time variation of the base flow. Using a time-varying base flow, the operator can be linearized around the base flow at each time. Thus, in this case, the operator and the base flow are time-varying. For instance, time-varying DMD (Zhang *et al.* 2019) addresses the time variation of the operator by applying weights to the dataset, considering only certain times or using only data from specific time ranges. Stankiewicz *et al.* (2017) proposed a method to continuously interpolate the DMD modes of early development, comparable to eigenmodes from GSA, with those of fully developed periodic flows. The change in base flow during the transient process is accomplished by correcting the mean field of stable periodic flow with the base flow at initial development (Noack *et al.* 2003), which is the steady-state flow satisfying the time-independent Navier–Stokes equation (Fornberg 1980). Note that rather than providing a model that aligns completely with the transient development of the actual flow, this is an approximation through interpolation. These methods can potentially describe the time variation of operators and their eigenmodes in transient processes. However, these methods are not extended to the energy transfer and budget analysis between different frequencies and viscous diffusion.

Resolvent analysis (Rolandi *et al.* 2024; Trefethen *et al.* 1993; Herrmann *et al.* 2021; Iwatani *et al.* 2023; Ballouz *et al.* 2024) is also a method for dealing with the development caused by energy amplification in transient flows. Considering the situation where the flow linearly develops from a specific base flow, resolvent analysis determines the optimal forcing that will maximize the energy amplification of the developed perturbation over a specific time span. An appropriate choice of time span and base flow can provide insights into energy transfer during the transient process. However, in practice, properly extracting the time-dependent variation in energy transfer during the growing process is difficult because the time-varying base flow and time span cannot be determined during the transient process.

Mode extraction based on time-varying operators provides a natural foundation for energy transfer analysis, as the decomposition is inherently frequency-based. Since DMD is formulated on frequency, it is less likely than POD to include multiple frequency components within a single mode. As a result, it is more suitable for analyzing energy transfer and budget across different scales. In this study, we focus on energy transfer and budget analysis in transient flow processes using an ROM constructed from the eigenmodes of time-varying operators. While the direction of this analysis is similar to the energy budget approach of Noack *et al.* (2003), which uses a POD-based ROM, our emphasis is on analyzing actual transient flow fields and developing an operator-based framework. To achieve this, we adopt a projection-based Galerkin model that incorporates the eigenmodes of the time-varying operator, utilizing the bi-orthogonality between DMD modes and their adjoint counterparts (Tu 2013), as proposed by Zhang & Wei (2017). This formulation enables a more accurate assessment of energy interactions among dynamically evolving modes during the transient process.

This paper explores the possibility of energy transfer analysis using operator eigenmodes with the adjoint-based Galerkin model and analyzes the energy transfer of transient flows. The manuscript is organized as follows. Section 2 describes the preparation strategy for the dataset used in mode extraction. This dataset is prepared through numerical simulations and incorporates time-stepping GSA (Ohmichi 2014; Ranjan *et al.* 2020). Additionally, a novel method is introduced for efficiently extracting modes from time-varying operators in transient flows. Section 3 derives a low-dimensional model based on the eigenmodes of the operators

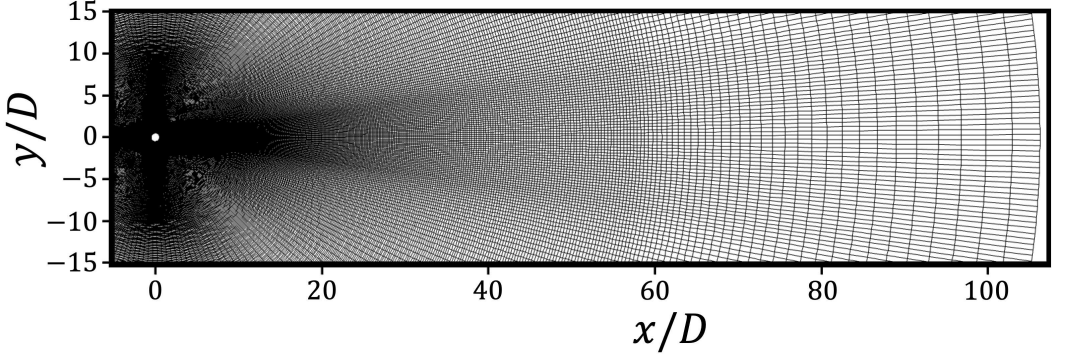


Figure 1: Computational grid around a circular cylinder.

and formulates energy transfer equations for analyzing the energy transfer and budget of transient flows. Section 4 deals with linear processes in which modes grow or decay from the steady field in two-dimensional cylinder flow covered by the GSA. The energy transfer analysis, using the equations developed in section 3, is applied to these linearly growing modes. Section 5 extends the analysis to nonlinear mode growth, investigating energy transfer and budget in flows that grow beyond the linear growth around the steady flow. Section 6 summarizes the main findings of this study.

## 2. Data preparation

### 2.1. Numerical method for solving governing equation

The flow around a circular cylinder was obtained from a numerical simulation of the incompressible Navier–Stokes equations. The governing equations are presented below.

$$\nabla \cdot \mathbf{u} = 0, \quad (2.1)$$

$$\frac{\partial \mathbf{u}}{\partial t} = -(\mathbf{u} \cdot \nabla) \mathbf{u} - \frac{1}{\rho} \nabla p + \frac{1}{Re} \nabla^2 \mathbf{u}, \quad (2.2)$$

where  $\mathbf{u}$  represents the velocity vector (bold symbols represent vectors),  $p$  is the pressure, and  $\rho$  is the fluid density. The  $Re$  is the Reynolds number defined as

$$Re = \frac{U_\infty D}{\nu}, \quad (2.3)$$

where  $U_\infty$  denotes the free-stream velocity,  $\nu$  is the kinematic viscosity, and  $D$  is the cylinder diameter.

The governing equations are solved by the fractional step method proposed by Le & Moin (1991). The time step size is determined based on our previous validation (Nakamura *et al.* 2024b). The second-order central difference (Kajishima & Taira 2017) and the QUICK method (Leonard 1979) were used for evaluating the spatial differences. The details of these numerical procedures are described in Nakamura *et al.* (2024a).

The computational grid is shown in figure 1. The grid convergence is provided in Appendix A. The far-field boundary of the computational grid is extended up to  $100D$ , which is used to ensure that the numerical results are not affected by the far boundary (Kumar & Mittal 2006). In the wall-normal direction, the number of grids was 240. In the wall-parallel direction, the number of grids was 590. The height of the first layer next to the cylinder was set at  $1.0 \times 10^{-3}D$  based on the DNS of Jiang & Cheng (2017).



## 2.2. GSA with time-stepping approach

The GSA is a practical approach to investigating the global stability in the base flow fields. From the perspective of the Hopf bifurcation behind a cylinder, the base flow represents steady fields, and global stability determines whether the perturbation in the wake Karman vortex grows or decays. The GSA considers time evolution of disturbances  $\tilde{\mathbf{u}}$  by the Navier–Stokes equations around a base flow:

$$\frac{d\tilde{\mathbf{u}}}{dt} = A\tilde{\mathbf{u}}, \quad (2.4)$$

where  $A$  denotes the operator around a base flow. The GSA aims to find the eigenvectors of matrix  $A$ . This study uses matrix-free GSA, which is referred to as a time-stepping approach (Ohmichi 2014; Ranjan *et al.* 2020). This method approximates the matrix  $A$  from the time evolution of the flow field with disturbances added to the base flow using numerical simulation.

A disturbance  $\tilde{\mathbf{u}}_0$  is initially prepared by

$$\tilde{\mathbf{u}}_0 = \epsilon_0 |\mathbf{u}_\Delta| \frac{\mathbf{r}_0}{|\mathbf{r}_0|}, \quad (2.5)$$

where  $|\cdot|$  represents the norm of the vector,  $\mathbf{u}_\Delta$  is the base flow,  $\mathbf{u}_0$  is the random disturbance, and  $\epsilon_0$  is a parameter that can be set to any value, representing the ratio of the baseflow and disturbance norms. The parameter dependence is provided in Appendix B. The flow field at  $t_0 + \Delta T$  after a time progression by the numerical simulation is presented below:

$$\mathbf{u}'_0(t_0 + \Delta T) = A'(\mathbf{u}_\Delta + \tilde{\mathbf{u}}_0), \quad (2.6)$$

$A'$  denotes the temporal evolution matrix obtained from numerical simulation,  $\mathbf{u}'_n(t_n + \Delta T)$  is the flow field after time evolution at  $t_n$ , and  $t_0$  represents the initial time. To collect data that approximates matrix  $A'$ , we iteratively compute the time progression of the flow field with disturbances added to the base flow. For the  $n$ th iteration ( $n > 1$ ), the disturbance  $\tilde{\mathbf{u}}_n$  to the base flow is computed from the flow field of  $(n - 1)$ th iteration presented below:

$$\tilde{\mathbf{u}}_n = \epsilon_0 |\mathbf{u}_\Delta| \frac{\mathbf{u}'_{n-1} - \mathbf{u}_\Delta}{|\mathbf{u}'_{n-1} - \mathbf{u}_\Delta|}. \quad (2.7)$$

The eigenvectors of matrix  $A$  can be computed by applying DMD to the following matrices

$$X = [\mathbf{u}_{N_s}, \mathbf{u}_{N_s+1}, \dots, \mathbf{u}_{M+N_s-1}] \in \mathbb{R}^{N \times M}, \quad (2.8)$$

$$X' = [\mathbf{u}'_{N_s}, \mathbf{u}'_{N_s+1}, \dots, \mathbf{u}'_{M+N_s-1}] \in \mathbb{R}^{N \times M}, \quad (2.9)$$

where  $N_s$  is the starting position of the DMD data and is set to remove the effect of snapshots with initial disturbance, and  $M$  is the number of snapshots. The DMD-based mode extraction in the time-stepping GSA is proposed by Ranjan *et al.* (2020). In this study,  $N_s$  is set to  $150D/(U_\infty \Delta T)$ .  $M$  is set such that  $N_s M - 1 = 50D/(U_\infty \Delta T)$  based on Nakamura *et al.* (2024a). A conceptual diagram of the mode extraction process using the time-stepping GSA is shown in figure 2.

## 2.3. DMD for mode extraction

DMD was proposed by Schmid (2010) to extract coherent structures from time series data of flow fields. This study computes eigenmodes from matrices  $X$  and  $X'$  obtained by time-stepping GSA based on an exact DMD algorithm (Tu 2013). The eigenmodes of matrix  $A$  are computed from  $X$  and  $X'$  as

$$A = X' X^\dagger, \quad (2.10)$$

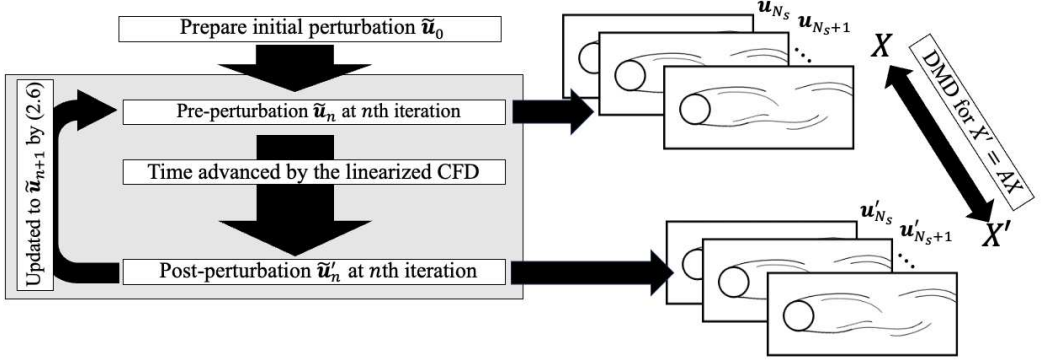


Figure 2: Schematic of time-stepping GSA using DMD.

where the superscript  $\dagger$  denotes the Moore–Penrose pseudoinverse. In the numerical processing,  $X$  is approximated by singular value decomposition (SVD)

$$X \approx U_r S_r V_r^T, \quad (2.11)$$

where  $U_r$  and  $V_r$  are the left and right singular vectors, respectively, and  $S_r$  is the diagonal matrix with non-negative diagonal elements (the singular values of  $X$ ). The matrix  $A$  is approximated by a low-rank matrix

$$\tilde{A} = U_r^T X' V_r S_r^{-1}, \quad (2.12)$$

where  $\tilde{A} = U_r^T A U_r$ .

The eigenvalue of matrix  $\tilde{A}$  represents the temporal evolution of the corresponding eigenvectors (eigenmode). The frequency and the growth rate are computed from

$$f_k = \frac{\text{Imag}\{\log(\lambda_k)\}}{2\pi\Delta T}, \quad (2.13)$$

$$\sigma_k = \frac{\text{Real}\{\log(\lambda_k)\}}{\Delta T}, \quad (2.14)$$

where  $\text{Real}(\cdot)$  and  $\text{Imag}(\cdot)$  represent the real and imaginary parts of the complex values, respectively, and  $\lambda_k$  is the eigenvalue of  $\tilde{A}$  corresponding to the  $k$ th eigenmode. The function  $\log(\cdot)$  denotes the complex logarithm, with the argument (phase angle) defined in the  $-\pi$  to  $\pi$ . In this paper, we denote the eigenmode for frequency  $f_k$  by  $\varphi_{f_k}$ . In the exact DMD, the eigenmodes  $\varphi_{f_k}$  is computed from the eigenmode  $\tilde{\varphi}_{f_k}$  of  $\tilde{A}$  as follows:

$$\varphi_{f_k} = X' V_r S_r^{-1} \tilde{\varphi}_{f_k}. \quad (2.15)$$

In this paper,  $f_k$  is indexed from  $k = 1$  in decreasing order of  $|f_k|$ , and negative frequency is denoted by  $f_{-k}$ .

#### 2.4. Mode extraction method for transient process using phase control

We extend time-stepping GSA to detect the nonlinear development of growth modes from steady fields. In the first iteration of the time-stepping method, the mode  $\varphi_{f_l}(\mathbf{x})$  with the largest growth rate is used as the initial disturbance, replacing the random perturbation typically employed. Note that in the two-dimensional cylinder case, the most amplified mode corresponds to the most dominant, lowest-frequency fluctuating component, i.e.,  $l = \pm 1$ . To provide perturbations to the developmental process, we introduce an initial temporal phase

$\alpha$  ( $0 \leq \alpha < 2\pi$ ). In summary, the initial flow field is given by

$$\mathbf{u}(\mathbf{x}, 0, \alpha) = \mathbf{u}_\Delta + \epsilon_0 |\mathbf{u}_\Delta| \{ e^{\alpha i} \boldsymbol{\varphi}_{f_l}(\mathbf{x}) + e^{-\alpha i} \boldsymbol{\varphi}_{f_l}(\mathbf{x}) \}. \quad (2.16)$$

Because of the nonlinear development of  $\boldsymbol{\varphi}_{f_l}$  and  $\mathbf{u}_\Delta$ , we do not update the fluctuating field in equation (2.7), and the operator from CFD is not linearized. Thus, time series data of the flow field from initial conditions controlled by  $\alpha$  are obtained as follows:

$$\mathbf{u}(\mathbf{x}, 0, \alpha), \mathbf{u}(\mathbf{x}, \Delta T, \alpha), \mathbf{u}(\mathbf{x}, 2\Delta T, \alpha), \dots, \mathbf{u}(\mathbf{x}, t, \alpha), \dots. \quad (2.17)$$

Here, we consider the average fields  $\mathbf{u}_\Delta(\mathbf{x}, t)$  over  $\alpha$ , defined as follows

$$\mathbf{u}_\Delta(\mathbf{x}, t) = \frac{1}{2\pi} \int_0^{2\pi} \mathbf{u}(\mathbf{x}, t, \alpha) d\alpha. \quad (2.18)$$

By linearizing the operator  $A$  around the  $\mathbf{u}_\Delta(\mathbf{x}, t)$ , time-varying linearized operator  $A(t)$  can be defined. Note that the initial operator  $A(0)$  equals the operator in the time-stepping GSA around the steady flow. Using this time-varying operator, time-series data is

$$\tilde{\mathbf{u}}(\mathbf{x}, 0, \alpha), A(0)\tilde{\mathbf{u}}(\mathbf{x}, 0, \alpha), A(\Delta T)\tilde{\mathbf{u}}(\mathbf{x}, \Delta T, \alpha), \dots, A(t)\mathbf{u}(\mathbf{x}, t, \alpha), \dots, \quad (2.19)$$

where  $\tilde{\mathbf{u}}(\mathbf{x}, t, \alpha)$  is

$$\tilde{\mathbf{u}}(\mathbf{x}, t, \alpha) = \mathbf{u}(\mathbf{x}, t, \alpha) - \mathbf{u}_\Delta(\mathbf{x}, t). \quad (2.20)$$

Now, we consider the eigenmode of the time-varying operator  $A(t)$ . In this case, the eigenmode is a function of  $\mathbf{x}$  and  $t$ . Thus, the  $\mathbf{u}(\mathbf{x}, t, \alpha)$  is decomposed into the result in time-variation of  $\mathbf{u}_\Delta(\mathbf{x}, t)$  and  $\boldsymbol{\varphi}_{f_k}(\mathbf{x}, t)$  presented below:

$$\mathbf{u}(\mathbf{x}, t, \alpha) = \mathbf{u}_\Delta(\mathbf{x}, t) + \sum_{f_k} \beta_{f_k}(t) e^{\sigma_k t + (2\pi f_k t - \alpha)i} \boldsymbol{\varphi}_{f_k}(\mathbf{x}, t), \quad (2.21)$$

where  $\beta_{f_k}(t)$  represents the amplitude of  $\boldsymbol{\varphi}_{f_k}(\mathbf{x}, t)$  corresponding to the flow field at that time. Note that, in this decomposition, frequency  $f_k$  and growth rate  $\sigma_k$  are also time-varying with the operator. It should also be noted that, even if the initial perturbation consists solely of the eigenvector corresponding to frequency  $f_1$ , nonlinear growth can lead to the emergence of multiple eigenvectors. These idea are similar to time-varying DMD (Zhang *et al.* 2019; Guan *et al.* 2024) and OTD decomposition (Zhong *et al.* 2025; Amiri-Margavi & Babaei 2024; Aitzhan *et al.* 2025).

We prepare the time-series data using equation (2.21) with discretized  $\alpha$  to  $j_{\max}$  points given by

$$\alpha_j = 2\frac{j-1}{j_{\max}}\pi. \quad (2.22)$$

Here, uniformly discretizing  $\alpha$  enables mode extraction with a small number of  $j_{\max}$ . The decomposition for mode is realized by applying exact DMD for the time-varying matrices  $X$  and  $X'$  presented below:

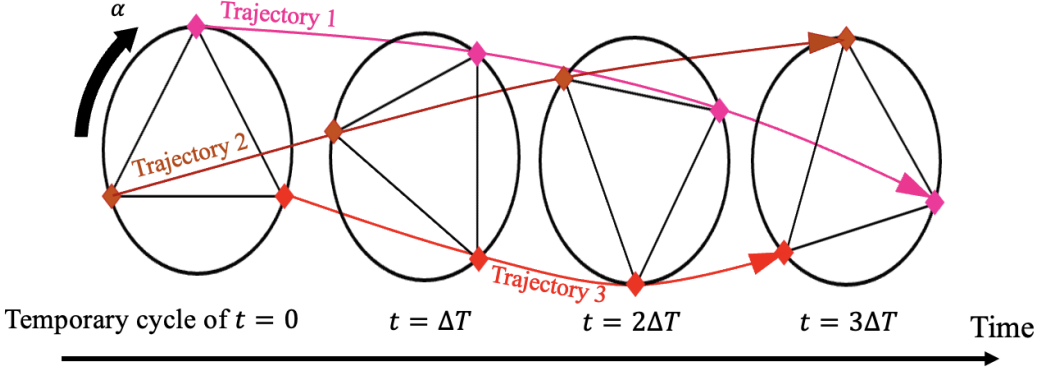
$$X(t) = [\mathbf{u}(\mathbf{x}, t, \alpha_1), \mathbf{u}(\mathbf{x}, t, \alpha_2), \dots, \mathbf{u}(\mathbf{x}, t, \alpha_{j_{\max}})] \in \mathbb{R}^{N \times j_{\max}}, \quad (2.23)$$

$$X'(t) = [\mathbf{u}(\mathbf{x}, t + \Delta T, \alpha_1), \mathbf{u}(\mathbf{x}, t + \Delta T, \alpha_2), \dots, \mathbf{u}(\mathbf{x}, t + \Delta T, \alpha_{j_{\max}})] \in \mathbb{R}^{N \times j_{\max}} \quad (2.24)$$

The schematic of this modal decomposition procedure is shown in figure 3. In this method, the phase of the dominant frequency  $f_1$  is controlled initially using a parameter  $\alpha$ , with the expectation that the phase of the solution trajectory will vary depending on  $\alpha$  at all times. As a result, the snapshot matrices at each time correspond to flow fields that are phase-shifted along the same cycle. We refer to this method as time-varying DMD with phase controlling (tDMDpc).



(a)



(b)

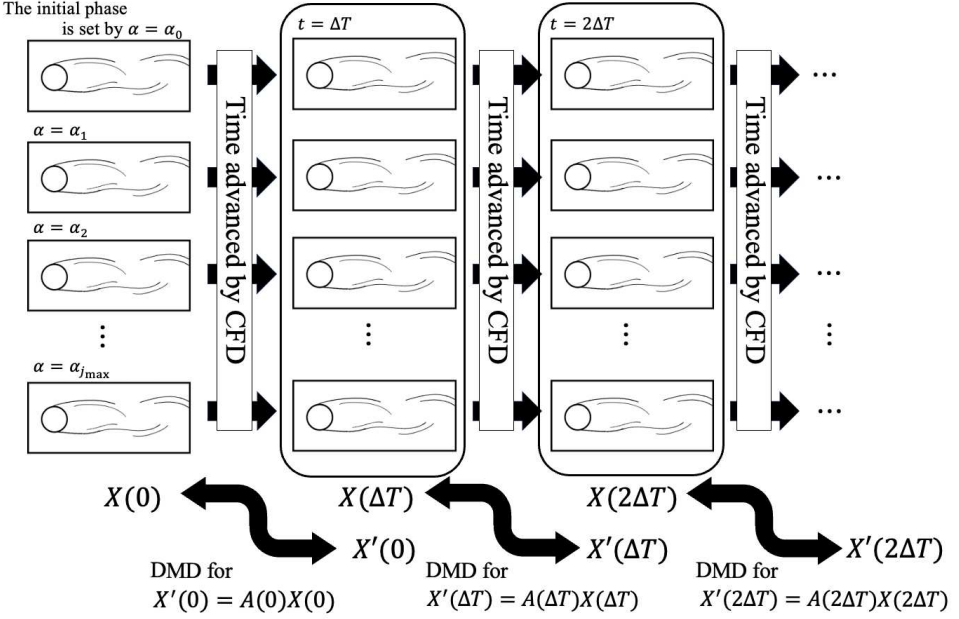


Figure 3: Schematic of tDMDpc. By changing the temporal phase of the mode in the initial flow and time progressing independently by CFD, a transient flow with different phases can be obtained.

Amplitude of eigenmode from tDMDpc  $|a_{f_k}|$  is computed as follows:

$$[b_{\Delta}(t, \alpha_j), b_{f_k}(t, \alpha_j), b_{f_k}^*(t, \alpha_j)] = [\mathbf{u}_{\Delta}, \boldsymbol{\varphi}_{f_k}(\mathbf{x}, t), \boldsymbol{\varphi}_{f_k}^*(\mathbf{x}, t)]^{\dagger} \mathbf{u}(\mathbf{x}, t, \alpha_j),$$

$$|a_{f_k}(t)| = \sum_{j=1}^{j_{\max}} \frac{|b_{f_k}(t, \alpha_j)|}{j_{\max}}, \quad (2.25)$$

where  $*$  represents the complex conjugate. In this paper, the Moore–Penrose pseudoinverse is computed by preconditioning the QR decomposition.

### 3. Model reduction approach and derivation of energy transfer equation

In this section, we describe a method for analyzing energy transfer and budget based on the Galerkin projection of the governing equations. Our goal is to derive the energy transfer between modes and the energy budget of each mode using the eigenmodes  $\boldsymbol{\varphi}_{f_k}$  and their corresponding coefficients  $a_{f_k}$ . The modal coefficients are computed directly from the dataset and the eigenmodes, without requiring time integration or numerical prediction.

#### 3.1. General derivation of Galerkin model with bi-orthogonality

The Galerkin model has been treated as a model reduction approach for low-dimensional representations of dynamical systems undergoing Hopf bifurcations (Noack & Eckelmann 1994a). The concept of the Galerkin model is to reformulate the governing equations in a low-dimensional form by decomposing the solution into basis functions. This study adapts the eigenmodes of the operator as the basis function and the Galerkin model based on the adjoint mode model proposed by Zhang & Wei (2017). The velocity field is assumed to be represented by the operator eigenmode  $\boldsymbol{\varphi}_{f_k}(\mathbf{x})$  presented below:

$$\mathbf{u}(\mathbf{x}, t) = \mathbf{u}_\Delta(\mathbf{x}) + \sum_{k=-r}^r a_{f_k}(t) \boldsymbol{\varphi}_{f_k}(\mathbf{x}), \quad (3.1)$$

where  $a_{f_k}$  represents the coupling coefficient for eigenmode which has  $f_k$ -frequency. Here, the  $\boldsymbol{\varphi}_{f_k}(\mathbf{x})$  does not depend on time. The  $\mathbf{u}_\Delta$  needs to satisfy the boundary condition. The negative index is the negative frequency and satisfies the following

$$-f_k = f_{-k}, \quad (3.2)$$

$$a_{f_{-k}} = (a_{f_k})^*. \quad (3.3)$$

The negative frequency is required to represent the real-value velocity field by the complex-valued mode. The frequency  $f_0$  means 0-frequency mode. When  $\mathbf{u}_\Delta$  differs from the base flow or time-averaged component of the flow field, a 0-frequency mode is required to reproduce the oscillations about the mean flow. This is referred to as mean-field correlation (Noack *et al.* 2003).

The equation (3.1) is substituted into governing equation (2.2) as follows:

$$\begin{aligned} \sum_{k=-r}^r \frac{da_{f_k}}{dt} \boldsymbol{\varphi}_{f_k} = & - \sum_{i=-r}^r \sum_{j=-r}^r a_{f_i} a_{f_j} (\boldsymbol{\varphi}_{f_i} \cdot \nabla) \boldsymbol{\varphi}_{f_j} \\ & - \sum_{i=-r}^r a_{f_i} \left\{ (\mathbf{u}_\Delta \cdot \nabla) \boldsymbol{\varphi}_{f_i} + (\boldsymbol{\varphi}_{f_i} \cdot \nabla) \mathbf{u}_\Delta + \frac{1}{Re} \nabla^2 \boldsymbol{\varphi}_{f_i} \right\} \\ & - (\mathbf{u}_\Delta \cdot \nabla) \mathbf{u}_\Delta + \frac{1}{Re} \nabla^2 \mathbf{u}_\Delta - \frac{1}{\rho} \nabla p. \end{aligned} \quad (3.4)$$

Here, we introduce an adjoint mode  $\boldsymbol{\varphi}_{f_k}^{\text{ad}}$  whose inner product with the  $f_k$ -frequency eigenmode is unity and which is orthogonal to the other eigenmodes (biorthogonal), represented by the following equation

$$\langle \boldsymbol{\varphi}_{f_i}, \boldsymbol{\varphi}_{f_j}^{\text{ad}} \rangle = \delta_{ij}, \quad (3.5)$$

where  $\delta_{ij}$  is the Kronecker delta. Note that the adjoint mode is the left eigenmode of  $A$  and can be computed from the right eigenmode of  $A^H$ , where the subscript  $H$  denotes the Hermitian transpose (Tu 2013). In equation (3.4), computing the inner product with the

$f_k$ -frequency adjoint mode, we obtain

$$\frac{da_{f_k}}{dt} = \sum_{i=-r}^r \sum_{j=-r}^r a_{f_i} a_{f_j} F_{f_i f_j f_k} + \sum_{i=-r}^r a_{f_i} G_{f_i f_k} + H_{f_k}, \quad (3.6)$$

where

$$F_{f_i f_j f_k} = -\langle (\boldsymbol{\varphi}_{f_i} \cdot \nabla) \boldsymbol{\varphi}_{f_j}, \boldsymbol{\varphi}_{f_k}^{\text{ad}} \rangle, \quad (3.7)$$

$$G_{f_i f_k} = \frac{1}{Re} \langle \nabla^2 \boldsymbol{\varphi}_{f_i}, \boldsymbol{\varphi}_{f_k}^{\text{ad}} \rangle - \langle (\mathbf{u}_\Delta \cdot \nabla) \boldsymbol{\varphi}_{f_i}, \boldsymbol{\varphi}_{f_k}^{\text{ad}} \rangle - \langle (\boldsymbol{\varphi}_{f_i} \cdot \nabla) \mathbf{u}_\Delta, \boldsymbol{\varphi}_{f_k}^{\text{ad}} \rangle, \quad (3.8)$$

$$H_{f_k} = \frac{1}{Re} \langle \nabla^2 \mathbf{u}_\Delta, \boldsymbol{\varphi}_{f_k}^{\text{ad}} \rangle - \langle (\mathbf{u}_\Delta \cdot \nabla) \mathbf{u}_\Delta, \boldsymbol{\varphi}_{f_k}^{\text{ad}} \rangle. \quad (3.9)$$

Note that the pressure term in the equation (3.4) is negligible in the cylinder flow (Ma & Karniadakis 2002; Noack *et al.* 2005).

### 3.2. Derivation of global energy transfer equation

We derive an equation that describes the energy transfer relationship between modes of different frequencies. Considering a triadic of two or three frequencies, the frequencies that interact with each other have the following relationship

$$f_o \mp f_p \pm f_q = 0. \quad (3.10)$$

In the ROM, interaction between different frequencies occurs through the coefficients  $F$  and  $G$ . Thus, the coefficients for frequencies that are not in a triadic relationship are

$$F_{f_i f_j f_k} = 0 \quad (f_k \neq f_i + f_j), \quad (3.11)$$

$$G_{f_i f_k} = 0 \quad (f_k \neq f_i), \quad (3.12)$$

$$H_{f_k} = 0 \quad (f_k \neq 0). \quad (3.13)$$

Note that the term associated with the negative frequency component must take the conjugate of the modes so that

$$F_{f_i f_j f_k} \neq F_{f_i f_{-j} f_k}, \quad (3.14)$$

$$G_{f_i f_k} \neq G_{f_{-i} f_k}. \quad (3.15)$$

This assumes that mode  $\boldsymbol{\varphi}_{f_k}$  oscillates at frequency  $f_k$ . In this context, equation (3.4) becomes

$$\frac{da_{f_k}}{dt} = \sum_{i=\max(k-r, -r)}^{\min(k+r, r)} (a_{f_i} a_{f_{k-i}} F_{f_i f_{k-i} f_k}) + a_{f_k} G_{f_k f_k} \quad (k \neq 0), \quad (3.16)$$

$$\frac{da_{f_0}}{dt} = \sum_{i=-r}^r (a_{f_i} a_{f_{-i}} F_{f_i f_{-i} f_0}) + a_{f_0} G_{f_0 f_0} + H_0 \quad (k = 0). \quad (3.17)$$

Here, the summation  $\sum_{i=\max(k-r, -r)}^{\min(k+r, r)}$  symbolically indicates that among the  $r$  frequencies, the nonlinear terms are summarized for frequencies in a triadic relationship with  $f_k$ .

To derive the energy transfer for the frequency  $f_k$ , we consider the time derivative of  $|a_{f_k}|^2$ . By mathematical deformation, we obtain

$$\frac{d}{dt} |a_{f_k}|^2 = a_{f_k}^* \frac{da_{f_k}}{dt} + a_{f_k} \frac{da_{f_k}^*}{dt} \quad (3.18)$$

$$= 2\text{Real} \left( a_{f_k}^* \frac{da_{f_k}}{dt} \right). \quad (3.19)$$

Therefore, the time derivative of energy satisfies the following equation

$$\frac{1}{2} \frac{d}{dt} |a_{f_k}|^2 = \sum_{i=\max(k-r, -r)}^{\min(k+r, r)} \text{Real}(a_{f_i} a_{f_{k-i}} a_{f_k}^* F_{f_i f_{k-i} f_k}) + \text{Real}(G_{f_k f_k}) |a_{f_k}|^2. \quad (3.20)$$

Here, since  $|a_{f_k}|^2$  represents the integral amount of energy over the entire field, equation (3.20) is the global energy transfer equation. Note that the first term of the right-hand side of equation (3.20) means the triadic interaction of  $f_i$ ,  $f_k$ , and  $f_{k-i}$ . The second term includes the diffusion effect and interaction with the base flow.

### 3.3. Around the steady flow

In the Hopf bifurcation, the flow field comprises a steady base flow and oscillators of frequency  $f_1$ . Hence, the reduction to the most straightforward system for Hopf bifurcation begins with expressing the velocity field as

$$\mathbf{u}(\mathbf{x}, t) = \mathbf{u}_\Delta(\mathbf{x}) + a_{f_1}(t) \boldsymbol{\varphi}_{f_1}(\mathbf{x}) + a_{f_{-1}}(t) \boldsymbol{\varphi}_{f_{-1}}(\mathbf{x}), \quad (3.21)$$

where  $\boldsymbol{\varphi}_{f_1}(\mathbf{x})$  does not depend on time since linear growth from the steady field is assumed. Since the nonlinear term is negligible due to linearization around the steady field, the dynamical system reduced by the Galerkin model is summarized below.

$$\frac{da_{f_1}}{dt} = a_{f_1} G_{f_1 f_1}. \quad (3.22)$$

Thus, frequency and growth rate of  $a_{f_1}$  is

$$\sigma_{f_1} = \text{Real}(G_{f_1 f_1}) \quad (3.23)$$

$$f_1 = \frac{\text{Imag}(G_{f_1 f_1})}{2\pi}. \quad (3.24)$$

The global energy transfer equation is

$$\frac{d}{dt} |a_{f_1}|^2 = 2\text{Real}(G_{f_1 f_1}) |a_{f_1}|^2 = 2\sigma_{f_1} |a_{f_1}|^2. \quad (3.25)$$

Generally, the following Landau equations describe the dynamical system of the Hopf bifurcation

$$\frac{dB}{dt} = \sigma B - B^3, \quad (3.26)$$

$$\frac{d\alpha}{dt} = \omega - bB^2, \quad (3.27)$$

where  $B$  denotes the amplitude of the oscillator ( $|a_{f_1}|$ ),  $\sigma$  is the growth rate of the oscillator at the equilibrium point, and  $\alpha$  is the oscillator's phase. In the context of the Landau equation, the squared amplitude is

$$\frac{dB^2}{dt} = 2B \frac{dB}{dt} = 2\sigma B^2 - 2B^4. \quad (3.28)$$

A comparison of the equation for the squared amplitude derived from the Landau equation with the global energy transfer equation (3.25) shows that the transfer equation has no fourth-order term for the amplitude. The fourth-order term in equation (3.28) has the effect of suppressing amplitude amplification due to its negative coefficient. This term stabilizes the oscillator at a specific limit cycle when it leaves the equilibrium point. Hence, the absence of a fourth-order term in the global energy transfer equation leads to energy divergence in the

reduced dynamical system. Noack *et al.* (2003) showed that correcting the steady field with oscillator amplification can suppress the divergence of the amplitude (mean-field correction). However, since the amplitude is close to 0 around the steady field, the effect of the fourth-order term is negligible. This indicates that the global energy transfer equation is a valid approximation at the steady state.

Moreover, the comparison of the coefficients of the second-order terms leads to the simple conclusion that the growth rate is equal to  $\text{Real}(G_{f_i f_i})$ . When kinetic energy is defined as  $\mathbf{u}^T \mathbf{u}$ , energy transfer represents  $2\sigma \mathbf{u}^T \mathbf{u}$ . That is, once  $\mathbf{u}$  is excited, the dynamical system acts as an amplifier of  $\mathbf{u}$ 's oscillation. Hence, the change in sign of the growth rate across the pre- and post-critical  $Re$  indicates a shift in the energy transfer direction. This simple conclusion connects dynamical systems and fluid dynamics. Note that for obtaining the structure that first transfers energy to  $\mathbf{u}$ , an approach based on the adjoint GSA (Giannetti & Luchini 2007; Luchini & Bottaro 2014; Ohmichi & Yamada 2021) or resolvent analysis is a reasonable choice.

### 3.4. For transient flow

We derive the energy transfer equation considering the time variation of the mode and frequency. Taking into account the time variation of the mode, equation (3.1) becomes

$$\mathbf{u}(\mathbf{x}, t) = \mathbf{u}_\Delta(\mathbf{x}, t) + \sum_{k=-r}^r a_{f_k} \boldsymbol{\varphi}_{f_k}(\mathbf{x}, t), \quad (3.29)$$

where, for  $k = 0$ ,  $a_{f_k} = 0$  since the time variation of the base flow (0-frequency mode) is already accounted for by  $\mathbf{u}_\Delta(\mathbf{x}, t)$ . In this case, the time derivative term of the mode is required because

$$\frac{d}{dt}(a_{f_k} \boldsymbol{\varphi}_{f_i}) = \boldsymbol{\varphi}_{f_i} \frac{da_{f_k}}{dt} + a_{f_k} \frac{d\boldsymbol{\varphi}_{f_i}}{dt}. \quad (3.30)$$

In this manner, equation (3.6) becomes

$$\frac{da_{f_k}}{dt} = \sum_{i=-r}^r I_{f_k f_i} a_{f_i} + J_{f_k} + \sum_{i=-r}^r \sum_{j=-r}^r a_{f_i} a_{f_j} F_{f_i f_j f_k} + \sum_{i=-r}^r a_{f_i} G_{f_i f_k} + H_{f_k}, \quad (3.31)$$

where

$$I_{f_k f_i} = -\left\langle \frac{d\boldsymbol{\varphi}_{f_i}}{dt}, \boldsymbol{\varphi}_{f_k}^{\text{ad}} \right\rangle, \quad (3.32)$$

$$J_{f_k} = -\left\langle \frac{d\mathbf{u}_\Delta}{dt}, \boldsymbol{\varphi}_{f_k}^{\text{ad}} \right\rangle. \quad (3.33)$$

We introduce the dynamic orthogonality condition for 0-mean stochastic process proposed by Sapsis & Lermusiaux (2009) in the reduced-order model for time-varying partial differential equations,

$$\left\langle \frac{d\boldsymbol{\varphi}_{f_i}}{dt}, \boldsymbol{\varphi}_{f_k}^{\text{ad}} \right\rangle = 0. \quad (3.34)$$

The term of  $J_{f_k}$  represents the time variation of the 0-frequency field, which can be neglected for non-zero  $f_k$ . In this manner, equation (3.35) is reduced to

$$\frac{da_{f_k}}{dt} = \sum_{i=-r}^r \sum_{j=-r}^r a_{f_i} a_{f_j} F_{f_i f_j f_k} + \sum_{i=-r}^r a_{f_i} G_{f_i f_k} + H_{f_k} \quad (k \neq 0), \quad (3.35)$$

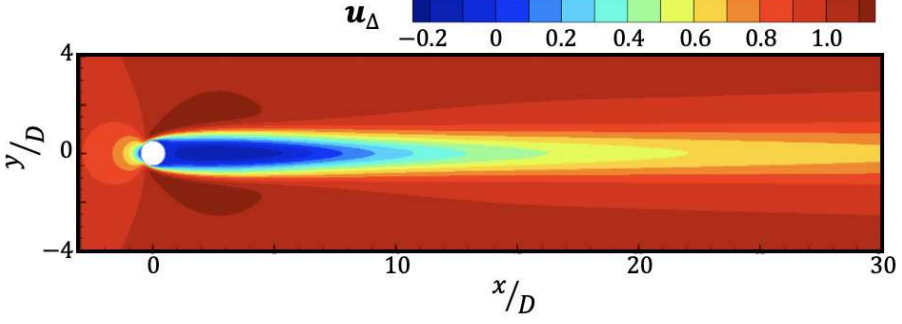


Figure 4: Streamwise velocity fields of the base flow at  $Re = 100$ . The base flow is obtained using the numerical technique of Nakamura *et al.* (2025a).

where  $F_{f_i f_j f_k}$ ,  $G_{f_i f_k}$ , and  $H_{f_k}$  are also time-varying.

Therefore, for  $k \neq 0$ , equation (3.35) is equivalent to equation (3.6). By considering the dynamic triadic relationship at arbitrary times,

$$f_o(t) \mp f_p(t) \pm f_q(t) = 0, \quad (3.36)$$

the global energy transfer equation for time-varying modes ( $k \neq 0$ ) becomes

$$\frac{1}{2} \frac{d}{dt} |a_{f_k}|^2 = \sum_{i=\max(k-r, -r)}^{\min(k+r, r)} \text{Real}(a_{f_i} a_{f_{k-i}} a_{f_k}^* F_{f_i f_{k-i} f_k}) + \text{Real}(G_{f_k f_k}) |a_{f_k}|^2. \quad (3.37)$$

This represents a time-varying energy budget that considers the time variation of energy.

#### 4. Energy transfer analysis around the steady flow

We analyze the energy transfer for decaying or growing modes using the global energy transfer equation linearized around a steady field for two-dimensional cylinder flow. In this section, we analyze time-independent modes derived from the equations linearized around a steady field. Thus, this section presents the energy transfer analysis for the GSA results.

##### 4.1. GSA results

The time-stepping GSA was performed for the flow around a cylinder. The base flow is computed by imposing symmetry on  $y = 0$  (Nakamura *et al.* 2025a). Figure 4 shows the streamwise velocity fields of the base flow at  $Re = 100$ . A recirculation region with negative streamwise velocity is formed in the cylinder wake. Many previous studies (Sen *et al.* 2009; Fornberg 1980) have reported that the recirculation region of the wake expands with increasing  $Re$ .

Figure 5 (a) shows the 0-lines of streamwise velocity for the base flow at various  $Re$ , which characterize the wake recirculation region. As the Reynolds number increases, the recirculation region becomes larger. Here, the length of the recirculation region,  $L_{\text{recirc}}$ , is defined as the  $x$ -position where the 0-line and  $y = 0$  intersect, excluding the cylinder surface. Figure 5 (b) shows the relationship between  $L_{\text{recirc}}$  and  $Re$ .  $L_{\text{recirc}}$  increases linearly with  $Re$ , in close agreement with the results of Sen *et al.* (2009).

The GSA was performed using the obtained base flow  $\mathbf{u}_\Delta$ . The details of the parameter choices in the time-stepping method are discussed in Appendix B. Figure 6 shows the modes with the most dominant eigenmode at  $Re = 40, 60, 100$ , and  $150$ , obtained from the results of the GSA, along with the absolute value of the modes. The 0 line of the base flow for the same



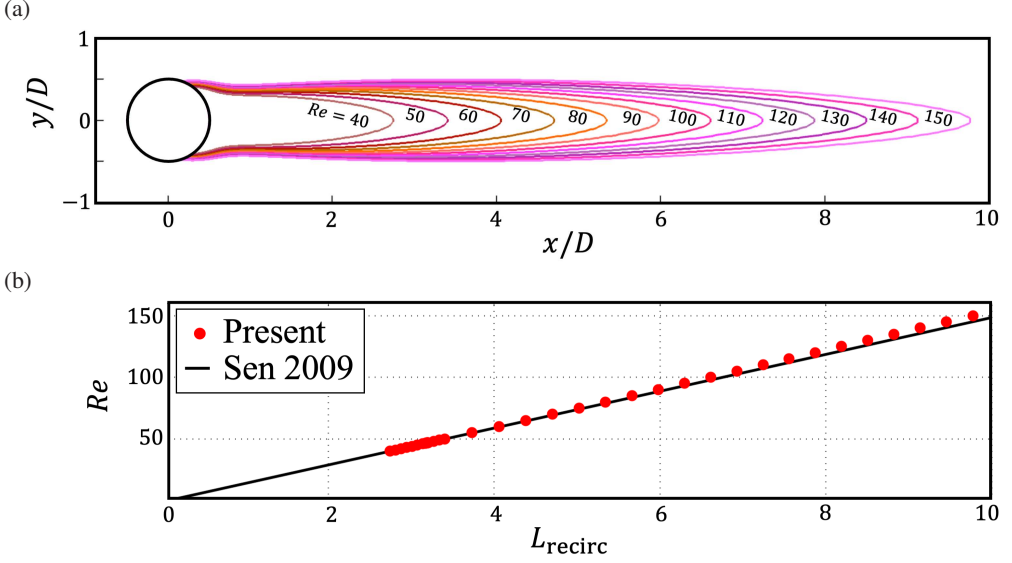


Figure 5: Base flow for various  $Re$ . (a) 0-line of the streamwise velocity component of the base flow (steady flow) at various  $Re$ . (b) The  $x$ -direction length of the recirculation region,  $L_{\text{recirc}}$ . The  $x$ -direction length of the 0 line expands linearly with increasing  $Re$ .

$Re$  values is shown in the figure as a black line. In the case of cylinder flow, the most dominant mode has the lowest frequency,  $f_1$ . Thus, the most unstable mode is referred to as  $\varphi_{f_1}$ . The spatial distribution of  $\varphi_{f_1}$  is asymmetric with respect to  $y = 0$  for all  $Re$  cases. Focusing on the distribution around the 0 line of the base flow, asymmetric fluctuations exist vertically above and below the recirculation region enclosed by the 0 line. This represents the beginning of forming an asymmetric Karman vortex that arises from a symmetric recirculation region.

The distribution of absolute values of  $\varphi_{f_1}$  is in good agreement with Giannetti & Luchini (2007); Mittal (2009). For  $Re > 60$ ,  $\varphi_{f_1}$  shows that the values become small sufficiently far from the cylinder. The peak value of  $|\varphi_{f_1}|$  occurs at approximately  $x/D \approx 10$ , except for  $Re = 40$ . However, this position does not follow a monotonous trend with respect to  $Re$ .

Figure 7 shows the growth rate of  $\varphi_{f_1}$  and the frequency  $f_1$  at each  $Re$ . The growth rate monotonically increases with increasing  $Re$ , and the sign of the growth rate changes at  $Re \approx 46.8$ . The sign of the growth rate indicates whether the most unstable mode grows from the base flow, which implies the onset of a Hopf bifurcation. Thus, the critical  $Re$  is 46.8, which is quite similar to previous studies (Ohmichi 2014; Williamson 1996; Kumar & Mittal 2006; Barkley 2006; Giannetti & Luchini 2007). The frequency increases up to  $Re = 65$  and then starts to decrease at that  $Re$ . This trend is consistent with previous studies. The frequency values are in close agreement with the results of Ohmichi (2014) but are slightly smaller than those of Barkley (2006) and Giannetti & Luchini (2007). The difference is possibly due to the GSA methodology, as Ohmichi's result is based on GSA using the time-stepping method (matrix-free method), while the other two results are obtained using the matrix method. As shown in Appendix B, the frequencies obtained by the time-stepping method are close to those obtained from numerical simulations. From this perspective, we conclude that the time-stepping method is reasonable.

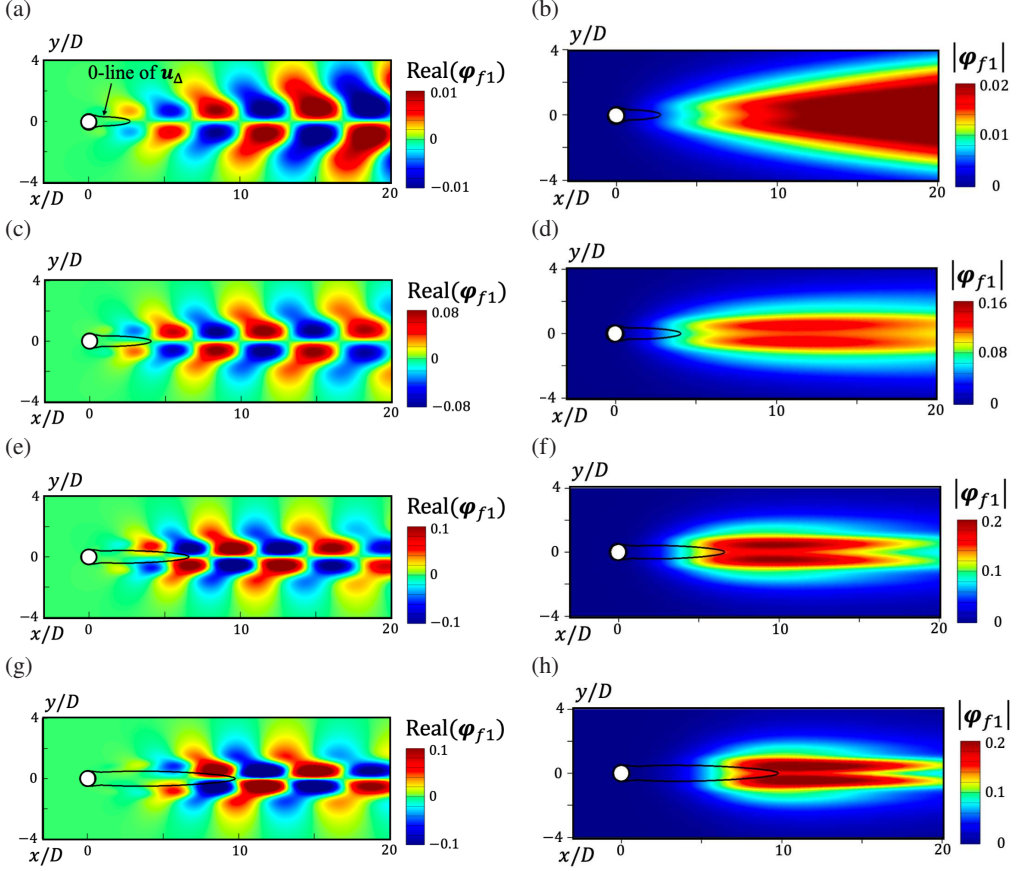


Figure 6: Spatial distribution of eigenmode  $\varphi_{f1}$  and its absolute value: (a) and (b)  $Re = 40$ , (c) and (d) 60, (e) and (f) 100, and (g) and (h) 150. The black line indicates the 0 line of streamwise velocity from the base flow.

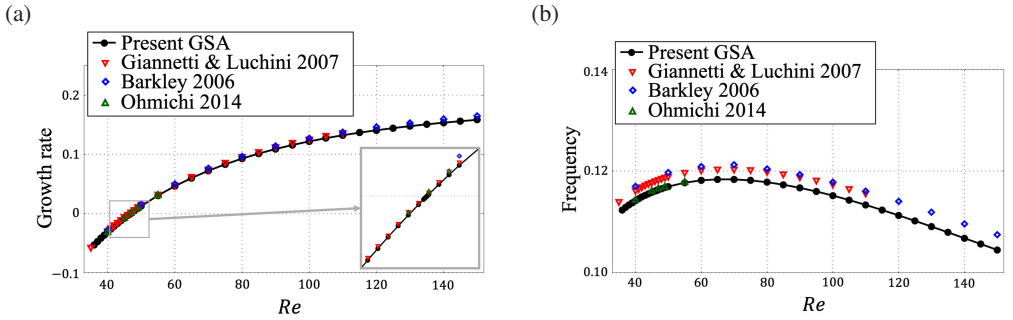


Figure 7: Comparison of (a) growth rate and (b) frequency obtained by the time-stepping GSA as a function of  $Re$  with previous works.

#### 4.2. ROM and energy transfer analysis

Galerkin-based ROM of the governing equations was conducted using the most unstable mode  $\varphi_{f1}$  and the base flow  $\mathbf{u}_\Delta$  at each  $Re$ . Using these modes, the growth rates in the ROM were computed based on equation (3.24). Figure 8 shows the growth rates and those obtained

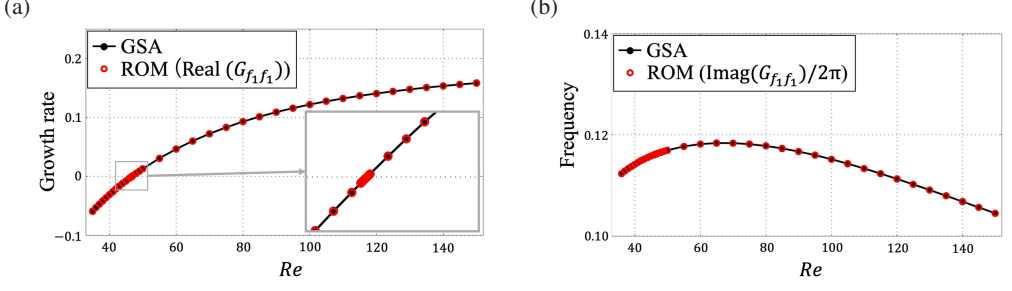


Figure 8: Comparison of growth rate and frequency between GSA and ROM, where growth rate and frequency of ROM are given by  $\text{Real}(G_{f_1 f_1})$  and  $\text{Imag}(G_{f_1 f_1})/(2\pi)$ , respectively. ROM closely approximates the growth rate and frequency of the eigenmode from GSA.

from GSA (indicated by the black line). The growth rates obtained from the ROM are in close agreement with the GSA results. Therefore, the ROM with base flow and unstable modes successfully reproduces the dynamical system around the base flow.

Here, we focus on the growth rate since it plays a significant role in the global energy transfer equation. From equation (3.24), the growth rate of the ROM is given by  $\text{Real}(G_{f_1 f_1})$ . The  $\text{Real}(G_{f_1 f_1})$  is expressed as the summation of three terms shown in equation (3.9). The term  $\frac{1}{Re} \langle \nabla^2 \varphi_{f_i}, \varphi_{f_i}^{\text{ad}} \rangle$  clearly represents the viscous diffusion term. In addition, the two nonlinear terms,  $-\langle (\mathbf{u}_\Delta \cdot \nabla) \varphi_{f_i}, \varphi_{f_i}^{\text{ad}} \rangle$  and  $\langle (\varphi_{f_i} \cdot \nabla) \mathbf{u}_\Delta, \varphi_{f_i}^{\text{ad}} \rangle$ , also contribute to  $G_{f_1 f_1}$ . From the momentum equation for the spectral energy budget (1.1),  $\varphi_{f_i}$  in the term  $(\varphi_{f_{n-l}} \cdot \nabla) \varphi_{f_i}$  acts as the donor of energy to the recipient  $\varphi_{f_n}$  (Freeman *et al.* 2024; Yeung *et al.* 2024). Therefore, we now define the real parts of the three terms, considering their origins, as follows:

$$\mathcal{D}_{f_i} = \frac{1}{Re} \text{Real}(\langle \nabla^2 \varphi_{f_i}, \varphi_{f_i}^{\text{ad}} \rangle), \quad (4.1)$$

$$\mathcal{T}_{f_i \rightleftharpoons f_i} = -\text{Real} \left\{ \langle (\mathbf{u}_\Delta \cdot \nabla) \varphi_{f_i}, \varphi_{f_i}^{\text{ad}} \rangle \right\}, \quad (4.2)$$

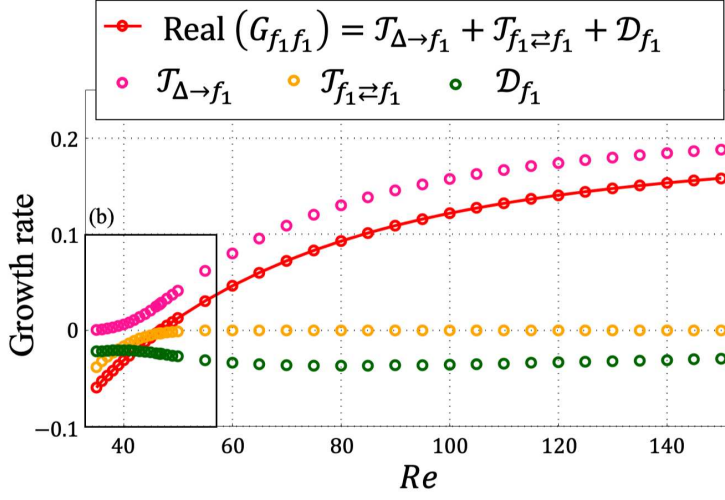
$$\mathcal{T}_{\Delta \rightarrow f_i} = -\text{Real} \left\{ \langle (\varphi_{f_i} \cdot \nabla) \mathbf{u}_\Delta, \varphi_{f_i}^{\text{ad}} \rangle \right\}, \quad (4.3)$$

where  $\mathcal{D}$  represents the diffusion term,  $\mathcal{T}$  is the transfer term, and the direction of the arrow in the subscript indicates the direction of energy transfer.

Figure 9 shows the values of the three terms computed numerically at each  $Re$ . Note that the red symbols in the figure represent the growth rate of the ROM, which is the sum of the three terms, as shown by the red symbols in figure 8. For all  $Re$  cases, only  $\mathcal{T}_{\Delta \rightarrow f_i}$  takes a positive value, indicating that  $\mathcal{T}_{\Delta \rightarrow f_i}$  is the term that amplifies the energy of  $\varphi_{f_i}$ . The diffusion term  $\mathcal{D}_{f_i}$  is always negative and remains nearly constant regardless of the  $Re$  value. Since  $\mathcal{D}_{f_i}$  has a coefficient of  $1/Re$ ,  $\text{Real}(\langle \nabla^2 \varphi_{f_i}, \varphi_{f_i}^{\text{ad}} \rangle)$  increases with  $Re$ . If  $\varphi_{f_i}$  is assumed to have a characteristic wavenumber, then  $\nabla^2 \varphi_{f_i}$  can be considered proportional to the square of that wavenumber. Consequently, the squared wavenumber would scale with the  $Re$ . However, as shown by the spatial distribution of the eigenmodes in Fig. 6, the wavenumber of the eigenmode is not necessarily uniform across the entire domain. Therefore, the relationship between wavenumber and  $Re$  remains speculative.

The term  $\mathcal{T}_{f_1 \rightleftharpoons f_1}$  is also negative for all  $Re$  cases, reflecting the effect of convection by the base flow (Mittal 2009). This indicates that energy is lost through convection, whereby  $\varphi_{f_i}$  transfers energy to itself. This self-decaying nature from convection is also reported by

(a)



(b)

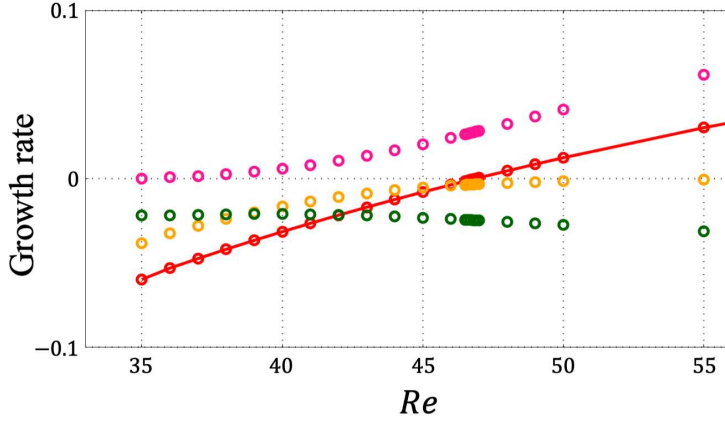


Figure 9: Individual plots of the three terms that comprise the ROM growth rate ( $\text{Real}(G_{f_1 f_1})$ ): (a) overall view, (b) close-up view around bifurcation point.

Yeung *et al.* (2024) in the post-transient, periodic cylinder flow at  $Re = 100$ . However, the slight negative values and resulting decay may indicate that energy is being advected out of the domain through the outflow boundaries. When the  $Re$  is smaller than the critical  $Re$ , this self-decaying property is more pronounced, and for  $Re < 39$ , it is smaller than the diffusion term. Therefore, it seems necessary to investigate not only viscous diffusion effects but also self-decaying mechanisms derived from convection by the base flow to understand the stable dynamics before bifurcation.

Going back to the fact that the value of each of the three terms is computed by the spatial integration, the spatial distribution of the integrated function determines the value of each term. This motivates us to define the spatial fields that determine the values of the three terms

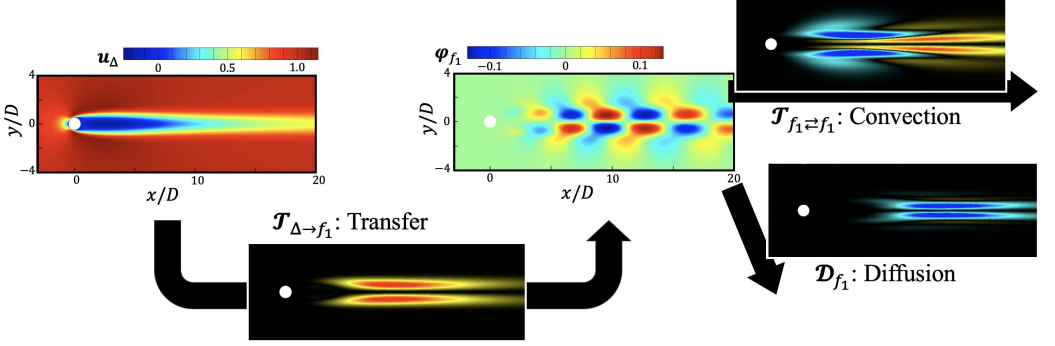


Figure 10: Diagram of energy transfer relationship of base flow  $u_\Delta$  and  $\varphi_{f_1}$  in the case of linearized system around the base flow. All contour map is the case of  $Re = 100$ , but this relationship is universal at least  $Re = 35$ – $150$  (see figure 9). The direction of the arrow indicates the signature of the integral value of the diffusion field and transfer field.

as follows:

$$\mathcal{D}_{f_1} = \frac{1}{Re} \text{Real}(\nabla^2 \varphi_{f_1} \circ \varphi_{f_1}^{\text{ad}}), \quad (4.4)$$

$$\mathcal{T}_{f_1 \rightleftharpoons f_1} = -\text{Real}(u_\Delta \cdot \nabla) \varphi_{f_1} \circ \varphi_{f_1}^{\text{ad}}, \quad (4.5)$$

$$\mathcal{T}_{\Delta \rightarrow f_1} = -\text{Real}((\varphi_{f_1} \cdot \nabla) u_\Delta \circ \varphi_{f_1}^{\text{ad}}), \quad (4.6)$$

inspired by the interaction map of BMD (Schmidt 2020) and the transfer field of TOD (Yeung *et al.* 2024). Here,  $\circ$  denotes the elementwise product. We refer to the spatial field  $\mathcal{D}_{f_1}$  as the diffusion field, and  $\mathcal{T}_{f_1 \rightleftharpoons f_1}$  and  $\mathcal{T}_{\Delta \rightarrow f_1}$  as transfer fields.

Figure 10 shows a conceptual diagram at  $Re = 100$ , considering three spatial field distributions:  $\mathcal{D}_{f_1}$ ,  $\mathcal{T}_{f_1 \rightleftharpoons f_1}$ , and  $\mathcal{T}_{\Delta \rightarrow f_1}$ , as well as the energy transfer direction determined by the sign of their spatial integrations:  $\mathcal{D}_{f_1}$ ,  $\mathcal{T}_{f_1 \rightleftharpoons f_1}$ , and  $\mathcal{T}_{\Delta \rightarrow f_1}$ . These distributions are in close agreement with those presented by Mittal (2009). Only  $\mathcal{T}_{\Delta \rightarrow f_1}$  acts as an amplifier, supplying energy, while the other two act as energy dampers. Therefore, whether  $\varphi_{f_1}$  develops or not depends on the sum of these three terms. The diffusion field  $\mathcal{D}_{f_1}$  is entirely negative, whereas  $\mathcal{T}_{\Delta \rightarrow f_1}$  shows an almost entirely positive distribution. In the field of  $\mathcal{T}_{f_1 \rightleftharpoons f_1}$ , both positive and negative value regions exist.

Transfer fields and diffusion fields for  $Re = 40, 60, 100$ , and  $150$  are shown in figure 11. The 0-line of the streamwise velocity for the base flow is shown for  $\mathcal{T}_{\Delta \rightarrow f_1}$ , and the contour lines of  $|\varphi_{f_1}|$  (see figure 6) are shown for the other fields by the white line. The diffusion field has a similar distribution to  $|\varphi_{f_1}|$ . This means that diffusion effects appear at all positions where fluctuations in the  $f_1$  frequency component exist. The transfer fields  $\mathcal{T}_{f_1 \rightleftharpoons f_1}$  exhibit a negative distribution near the cylinder and a positive distribution farther away from the cylinder, except for  $Re = 40$ . Compared to the distribution of  $|\varphi_{f_1}|$ , the distribution of  $\mathcal{T}_{f_1 \rightleftharpoons f_1}$  switches between positive and negative values around the peak- $x$  position of  $|\varphi_{f_1}|$ . These positive and negative regions cancel each other out, resulting in a net small negative transfer,  $\mathcal{T}_{f_1 \rightleftharpoons f_1}$ . Moreover, the presence of positive values in the far wake at  $Re = 60, 100$ , and  $150$  suggests that convection by the base flow contributes to the growth of the Karman vortices.

The transfer field  $\mathcal{T}_{\Delta \rightarrow f_1}$  has a distribution along the  $x$ -direction of the recirculation region, bounded by the 0-line. This distribution is very similar to the sensitivity region where fluctuations are caused by the wake recirculation region, as reported by Ohmichi & Yamada (2021). Since  $\mathcal{T}_{\Delta \rightarrow f_1}$  represents the energy transfer from the base flow to  $\varphi_{f_1}$ , the formation

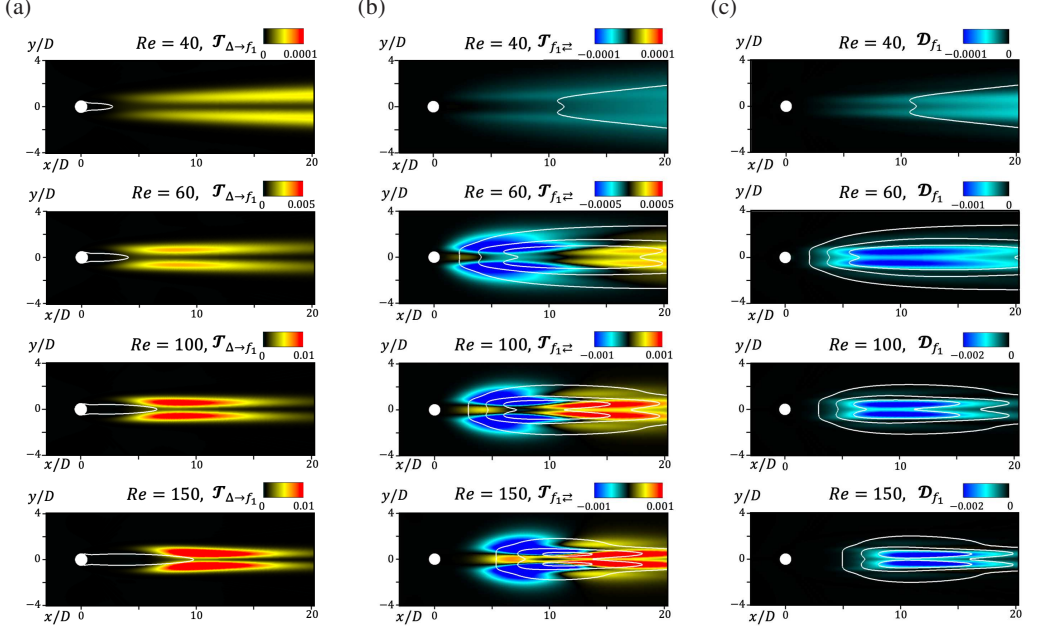


Figure 11: Spatial distribution of transfer fields and diffusion fields at  $Re = 40, 60, 100$ , and  $150$ .

of  $\varphi_{f_1}$  originates from the recirculation region of the base flow. Therefore, the growth of  $\varphi_{f_1}$  is driven by instability in the recirculation region of the wake. However, at  $Re = 40$ , this energy transfer is minimal, which is also evident from the integral value in figure 9. As  $Re$  increases, the length of the recirculation region also increases (see figure 5), making the wake recirculation more unstable and enhancing the energy transfer to  $\varphi_{f_1}$ .

## 5. Energy transfer and budget analysis for transient flow

The global energy transfer equation, linearized system around the steady field, successfully captures the system's dynamics near the steady field obtained from GSA. This section extends the transfer analysis to a transient nonlinear development process beyond the linear growth from the steady field. In such cases, the linearized energy transfer equation (3.25) alone cannot fully describe the evolution of the solution (Stankiewicz *et al.* 2017). Moreover, both the spatial distribution and frequency of the modes change throughout the transient process. Therefore, we extract the variations in the spatial distribution and frequency of the modes during the transient process using tDMDpc and analyze the corresponding energy transfer dynamics. We aim to provide a more comprehensive understanding of how energy transfers between different frequency components as the flow evolves from the steady field to its post-transient state.

### 5.1. tDMDpc result for cylinder flow

The transient flow process around a cylinder is decomposed using tDMDpc, with modes obtained from time-stepping GSA around a steady field. The parameters  $\Delta T$  and  $\epsilon_0$  are set to 0.1 and 0.001, respectively, which are the same values used in the time-stepping GSA. The initial perturbation fields at  $\alpha = 0, \pi/2, \pi$  for  $Re = 100$  are shown in figure 12. According to equation (2.16), the initial perturbation field at  $\alpha = 0$  corresponds to the real part of the



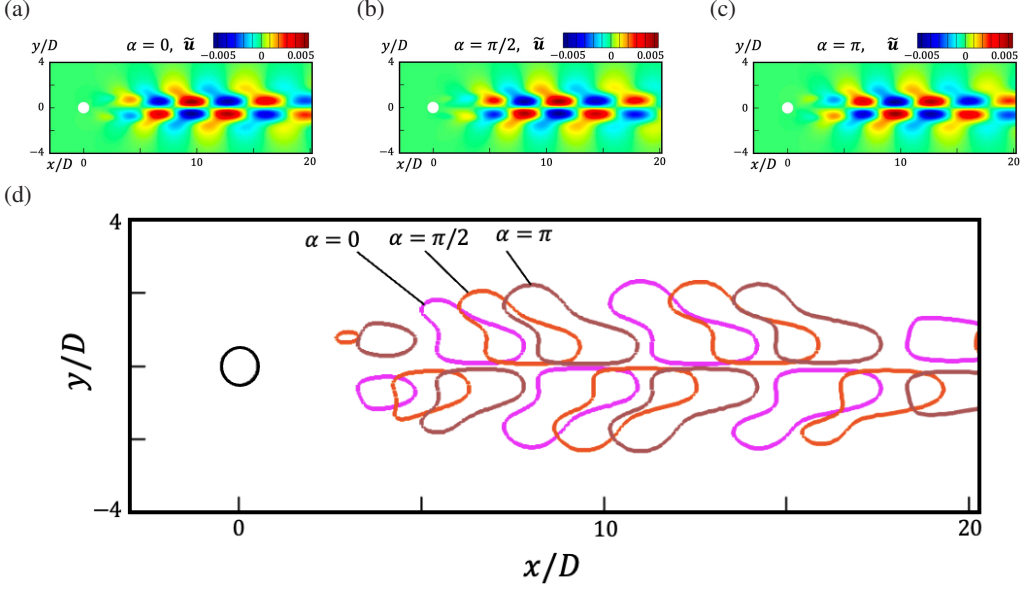


Figure 12: Initial perturbation fields of tDMDpc at  $Re = 100$  (a)  $\alpha = 0$ , (b)  $\alpha = \pi/2$ , (c)  $\alpha = \pi$ , and (d) contour lines of 0.001 at  $\alpha = 0, \pi/2$ , and  $\pi$ .

eigenmode, with its absolute value scaled by  $\epsilon_0$ . Thus, the spatial distribution in figure 12 (a) is identical to that in figure 6 (e). The initial perturbation field at  $\alpha = \pi/2$  corresponds to the imaginary part of the eigenmode, also scaled by  $\epsilon_0$ . The initial perturbation field at  $\alpha = \pi$  is equivalent to that at  $\alpha = 0$  but with the sign inverted. Figure 12 (d) presents an overlay plot of the contours at 0.001 for the three fields. The spatial distribution of the perturbation field changes depending on the value of  $\alpha$ , indicating that the phases of the oscillations differ.

The initial perturbation fields are prepared by varying the value of  $\alpha$  under  $j_{\max} = 20$ . Figure 13 shows the time variation of the transverse velocity at the wake position  $(x/D, y/D) = (1, 0)$ , computed from numerical simulations using the initial perturbation fields presented in figure 12. At  $t = 0$ , the velocity variation is too small to be significant, but as time progresses, the velocity perturbation grows. Once the oscillation amplitude reaches a sufficiently large value, it stabilizes, and the flow field transitions to the post-transient state. A comparison of flow fields for different  $\alpha$  values reveals that the oscillation phase shifts with respect to  $\alpha$ . Therefore, time-series data of flow fields evolving from initial conditions with varying  $\alpha$  provide the dataset of the development process with different temporal phases.

Using the time-series data of the flow field developed from  $j_{\max} = 20$  different  $\alpha$  values, we computed the flow field averaged over  $\alpha$  by (2.18) for snapshots at the same  $t$ . The number of snapshots,  $j_{\max}$ , in tDMDpc, corresponds to the number of snapshots used for averaging and mode extraction. Therefore, a sufficiently large number of snapshots is required for accurate results. The convergence of the averaged fields and the modes extracted by tDMDpc with respect to  $j_{\max} = 20$  is discussed in Appendix C. Figure 14 shows the 0-contour line of the streamwise velocity in the flow field averaged over  $\alpha$  at various times. The length of the recirculation region, bounded by the 0-contour line, decreases as time progresses.

Time-varying modes and eigenvalues were extracted using tDMDpc from the time-series data obtained with  $j_{\max} = 20$ , as illustrated in the conceptual diagram in figure 3 (b). Figure 15 shows the distribution of the eigenvalues of tDMDpc at times  $t = 30, 40, 55, 80$ . These times were chosen based on the variation in the length of the recirculation region (see figure

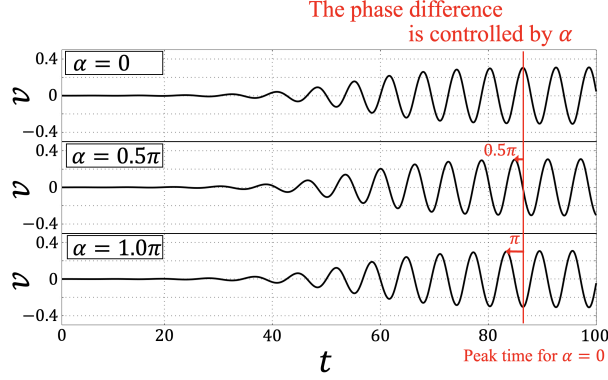


Figure 13: Time variation of transverse velocity component at  $(x/D, y/D) = (1, 0)$  at  $Re = 100$ , with different  $\alpha$  in tDMDpc. The temporal phase in the transient process can be controlled by  $\alpha$ .

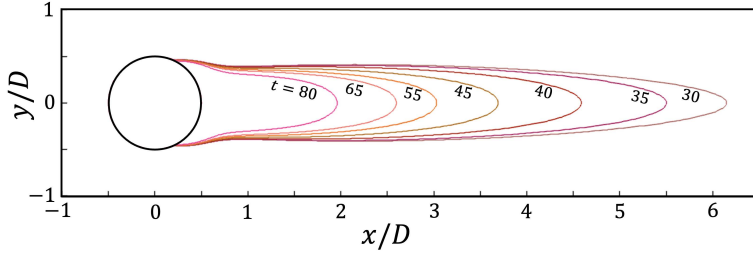


Figure 14: 0 line for streamwise velocity fields (recirculation region) at various times averaged over  $\alpha$  in the tDMDpc. The  $Re$  is 100. As flow fields develop, the recirculation region and length to the  $x$ -direction becomes small.

14). The eigenvalues that exist on the unit circle, indicated by the black line in the figure, correspond to a 0 growth rate. At  $t = 30$  and 40, a large number of eigenvalues are found outside the unit circle, indicating that the flow fields are growing. As time progresses, the eigenvalues concentrate around the unit circle, suggesting that the flow field converges to a stable quasi-steady state. The few eigenvalues located inside the unit circle are likely numerical errors near the outflow boundary.

The declination of each eigenvalue for the  $x$ -axis corresponds to the angular frequency. At  $t = 30$ , the eigenvalues with the lowest angular frequency, except for the 0-frequency, closely match the eigenvalues of the most unstable mode  $\varphi_{f_1}$  obtained from GSA. Therefore, the eigenvalues with the smallest angular frequency result from the nonlinear growing of the most unstable modes of GSA, which were used in the initial perturbation fields. Excluding numerical errors, it can be observed that the other frequencies correspond to harmonics of the  $f_1$  frequency. This behavior arises from the nonlinear interaction between the  $\varphi_{f_1}$  mode and other finite-frequency modes, leading to the appearance of modes with frequencies  $f_n = f_{n-1} + f_1$  for  $n = 2, 3, \dots$ .

Figure 16 presents the eigenmodes obtained from tDMDpc at frequencies  $0.1 < f_1 < 0.2$ ,  $f_2 = 2f_1$ , and  $f_3 = 3f_1$ , extracted at  $t = 30, 40, 55$ , and 80. The black line indicates the 0-contour line of the averaged fields over  $\alpha$ . For all three frequency components, as the recirculation region length decreases, the mode distribution gradually approaches to a cylinder. At  $t = 80$ , the well-known mode distributions for periodic flow around a cylinder, as reported in several studies (Sato & Schmidt 2025; Akhtar 2008; Yeung *et al.*

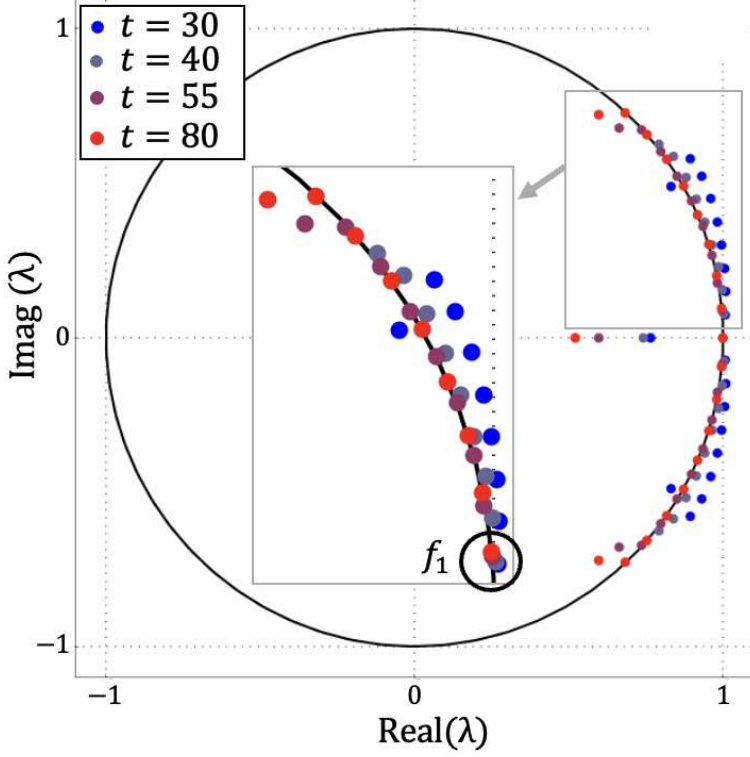


Figure 15: Eigenvalue distribution of tDMDpc at  $Re = 100$ . The black line represents the unit circle, which indicates the 0-growth rate. Flow fields become a stable state because the eigenvalue converges to the unit circle as time progresses.

2024; Noack *et al.* 2003; Taira *et al.* 2020; Tu 2013; Zhang & Wei 2017), are clearly visible. At  $t = 30$ , the fluctuation magnitude at a downstream location (e.g.,  $x/D \sim 10$ ) just beyond the recirculation region is comparable to that observed near the end of the recirculation region. However, as time advances, the fluctuations in the downstream region decay more rapidly, while those near the recirculation region persist or even intensify. These variations clearly depict the gradual evolution of the fluctuation field throughout the transient process, approaching the modes of the post-transient flow. Therefore, tDMDpc is an effective tool for extracting coherent structures during the transient process.

We perform tDMDpc for  $Re$  values other than 100 to investigate the dependance of flow variation on  $Re$ . For  $Re \approx 150$ , the vortex street transitions to a secondary vortex in the post-transient flow (Taneda 1959; Jiang & Cheng 2019). In this case, the wake vortex is no longer composed solely of harmonics of  $f_1$ . However, since the scope of this study focuses on the transient process from a steady flow, the secondary vortex falls outside the focus of this work. Therefore, this study addresses the transient process only for  $Re \leq 100$ , which is sufficiently smaller than 150.

For  $Re = 50, 60$ , and  $75$ , initial fields were prepared using the eigenmode from GSA with  $j_{\max} = 20$  for each  $Re$ , and time-series data for the transient process were obtained. From these transient data, we computed the flow field averaged over  $\alpha$  as described in (2.18) for each  $Re$ . Figure 17 illustrates the temporal evolution of the recirculation region length,  $L_{\text{recirc}}$ , in the averaged flow field for  $Re = 50, 60, 75$ , and  $100$ . For all  $Re$  values,  $L_{\text{recirc}}$  decreases over time. After a sufficiently long growth, the recirculation region stabilizes at a constant

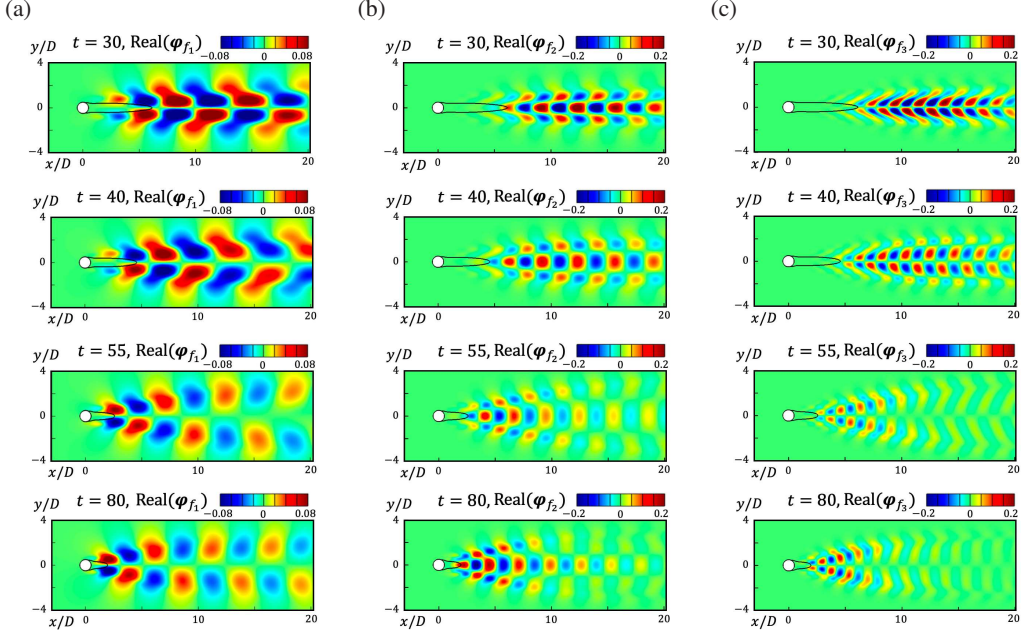


Figure 16: Time variation of eigen modes distribution from tDMDpc for (a) most lowest-frequency  $f_1$ , (b)  $f_2 = 2f_1$ , and (c)  $f_3 = 3f_1$ .

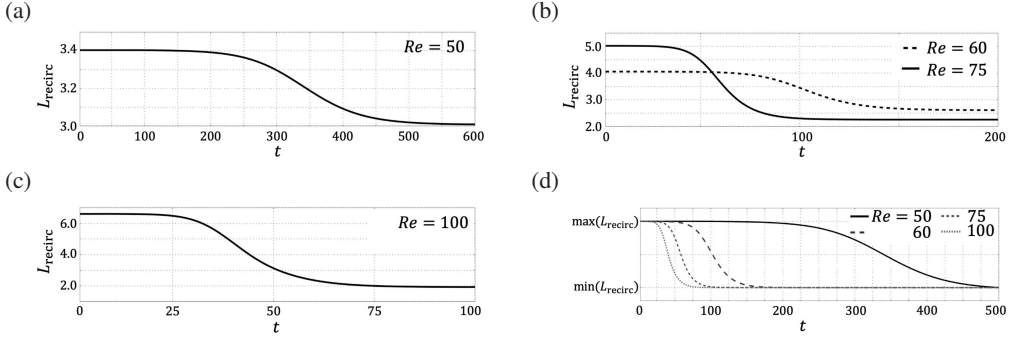


Figure 17: Time variation of  $L_{\text{recirc}}$  in the transient process: (a)  $Re = 50$ , (b) 60 and 75, (c) 100, and (d)  $Re = 50, 60, 75$ , and 100, normalized by the maximum and minimum  $L_{\text{recirc}}$ .

length, although the time required to reach this steady state is longer for smaller  $Re$  values. Figure 17 (d) presents a normalized plot of  $L_{\text{recirc}}$  for the four  $Re$  cases, where the vertical axis is scaled by the maximum and minimum lengths of the respective recirculation regions. The temporal variation trends of  $L_{\text{recirc}}$  are remarkably similar across all  $Re$  cases.

We performed tDMDpc using time-series data of transient processes at four  $Re$  values and extracted time-varying modes along with their growth rates. A gradual variation in the mode distribution over time was observed for all four  $Re$  values; however, for simplicity, the mode distributions are omitted here. For a more quantitative analysis, Figure 18 shows the time variation of the growth rates of the  $f_1$ -frequency mode at the four  $Re$  values. The growth rate gradually decreases over time and eventually reaches 0. This indicates that the perturbation field, which grows rapidly around the steady field, ultimately converges to a stable periodic flow. The trend in the time variation of the growth rates closely resembles the time variation

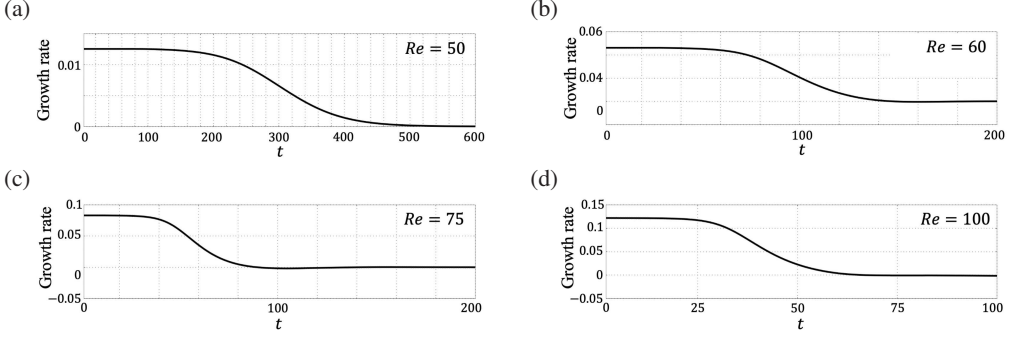


Figure 18: Time variation of growth rate in the transient process: (a)  $Re = 50$ , (b) 60, (c) 75, and (d) 100.

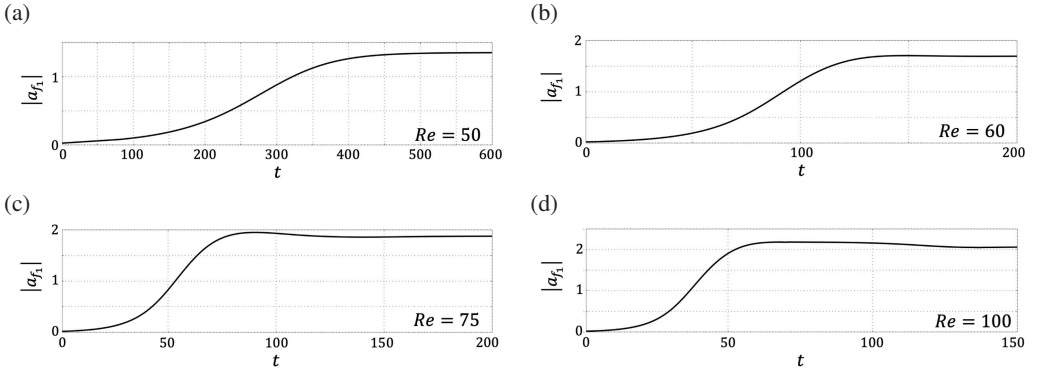


Figure 19: Time variation of mode amplitude  $|a_{f_1}|$ : (a)  $Re = 50$ , (b) 60, (c) 75, and (d) 100.

of the recirculation region. This suggests a potential connection between the recirculation region and the growth of perturbation fields. Since the growth rate is directly linked to energy transfer, as derived from the global energy transfer equation, investigating energy transfer in transient processes could provide further insight into these potential relationships.

### 5.2. Energy transfer properties in transient process

To investigate the time variation of the energy at arbitrary times in the transient process, we computed the amplitudes of eigenmodes from tDMDpc. Figure 19 shows the time variation of amplitude  $|a_{f_1}|$  at  $Re = 50, 60, 75$ , and 100 computed from equation (5.3) using tDMDpc mode. The amplitude increases over time during the transient process and eventually converges to a stable constant. This is consistent with the convergence of the growth rate to 0 in tDMDpc. The growth process is monotonically increasing for  $Re = 50$  and 60, whereas a temporary maximum is observed at  $Re = 75$  and 100.

In the global energy transfer equation (3.37), the nonlinear triadic term related to  $F_{f_i f_j f_k}$  is necessary to compute in the nonlinear case. Here, we define the nonlinear term as follows:

$$\mathcal{N}_{f_k} = \sum_{i=\max(k-r, -r)}^{\min(k+r, r)} \text{Real}(a_{f_i} a_{f_{k-i}} a_{f_k}^* F_{f_i f_{k-i} f_k}), \quad (5.1)$$

By the Galerkin projection, the high-frequency modes are truncated, and the triadic term cannot be directly computed. Therefore, we evaluate the term of  $\mathcal{N}_{f_k}$  using the global energy

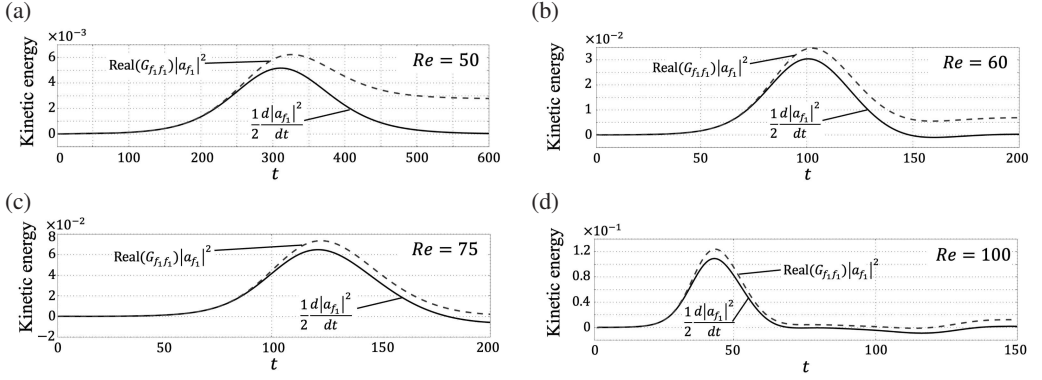


Figure 20: Time variation of kinetic energy for  $f_1$ -frequency mode  $d|a_{f_1}|^2/2dt$ , and energy transfer derived from linear term  $\text{Real}(G_{f_1 f_1})|a_{f_1}|^2$ : (a)  $Re = 50$ , (b) 60, (c) 75, (d) 100. Difference of  $d|a_{f_1}|^2/2dt$  and  $\text{Real}(G_{f_1 f_1})|a_{f_1}|^2$  is equal to triadic energy transfer.

transfer equation as follows

$$\mathcal{N}_{f_k}(t) = \frac{1}{2} \frac{d|a_{f_k}(t)|^2}{dt} - \text{Real}(G_{f_k f_k})|a_{f_k}(t)|^2 \quad (5.2)$$

where the time variation of energy can be computed by forward differencing from the mode amplitude presented below

$$\frac{d|a_{f_k}(t)|^2}{dt} = \frac{|a_{f_k}(t + \Delta T)|^2 - |a_{f_k}(t)|^2}{\Delta T}. \quad (5.3)$$

Figure 20 shows the time variation of the time derivative of energy and  $\text{Real}(G_{f_1 f_1})|a_{f_1}|^2$  computed from the eigenmode of tDMDpc at  $Re = 50, 60, 75$ , and 100. At each of the four  $Re$  values, the time variation of energy is temporarily maximal during the transient process. After sufficient evolution, the time variation of energy becomes 0, but  $\text{Real}(G_{f_1 f_1})|a_{f_1}|^2$  converges to a positive value. These values differ due to the energy transfer of  $\mathcal{N}_{f_k}$ .

Figure 21 shows the time variation of  $\mathcal{N}_{f_1}$ , computed as the difference between  $d|a_{f_1}|^2/2dt$  and  $\text{Real}(G_{f_1 f_1})|a_{f_1}|^2$ . The energy transfer remains negative across all times, indicating that energy is consistently transferred to higher-frequency modes. Since  $f_1$  is the lowest frequency in the eigenvalue distribution of tDMDpc,  $\mathcal{N}_{f_1}$  represents energy transfer to higher-frequency modes. Thus, the negative value confirms a totally forward cascade process, where energy is transferred from  $f_1$  to its harmonics.

Focusing on the time variation, for  $Re = 50$  and 60,  $\mathcal{N}_{f_1}$  decreases monotonically throughout the transient process. In contrast, for  $Re = 75$  and 100,  $\mathcal{N}_{f_1}$  reaches a temporary minimum before increasing and stabilizing in the steady state. These results indicate that nonlinearity becomes more pronounced as  $Re$  increases.

To investigate the variation of energy transfer in transient processes, we decompose  $\text{Real}(G_{f_1 f_1})$  into three terms:  $\mathcal{D}_{f_1}$ ,  $\mathcal{T}_{\Delta \rightarrow f_1}$ , and  $\mathcal{T}_{f_1 \rightleftharpoons f_1}$ , following the energy transfer analysis around a steady field. These terms are computed from  $\varphi_{f_1}(t)$  at each time step, and the corresponding values  $\mathcal{D}_{f_1}|a_{f_1}|^2$ ,  $\mathcal{T}_{\Delta \rightarrow f_1}|a_{f_1}|^2$ , and  $\mathcal{T}_{f_1 \rightleftharpoons f_1}|a_{f_1}|^2$  are obtained using time-varying  $\mathcal{D}_{f_1}(t)$ ,  $\mathcal{T}_{\Delta \rightarrow f_1}(t)$ ,  $\mathcal{T}_{f_1 \rightleftharpoons f_1}(t)$ , and  $a_{f_1}(t)$ . Here, it should be noted that the factor  $|a_{f_1}|^2$  is introduced to match the magnitude of the energy.

Figure 22 illustrates the time variation of the terms on the right-hand side of the global energy transfer equation (3.37):  $\mathcal{D}_{f_1}|a_{f_1}|^2$ ,  $\mathcal{T}_{\Delta \rightarrow f_1}|a_{f_1}|^2$ ,  $\mathcal{T}_{f_1 \rightleftharpoons f_1}|a_{f_1}|^2$ , and  $\mathcal{N}_{f_1}$ . Here,  $\mathcal{N}_{f_1}$



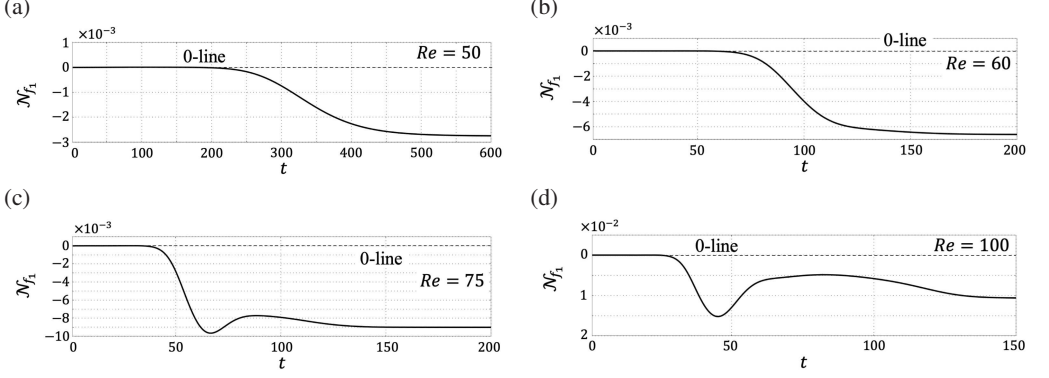


Figure 21: Time variation of difference between  $d|a_{f_1}|^2/2dt$ , and  $\text{Real}(G_{f_1 f_1})|a_{f_1}|^2$  (triadic energy transfer): (a)  $Re = 50$ , (b) 60, (c) 75, and (d) 100. Triadic energy transfer decreases monotonically at  $Re = 50$  and 60. Above  $Re = 75$ , it reaches a minimum value in a transient process and remains constant after increasing.

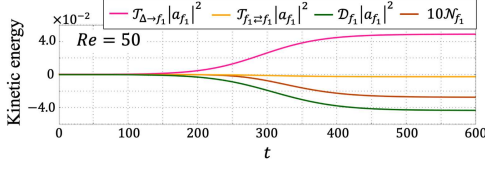
is plotted at 10 times its actual value to facilitate comparison with the other terms. Since  $\mathcal{T}_{\Delta \rightarrow f_1}|a_{f_1}|^2$  is positive, while  $\mathcal{T}_{f_1 \rightleftharpoons f_1}|a_{f_1}|^2$  and  $\mathcal{D}_{f_1}|a_{f_1}|^2$  are negative, the energy transfer relationships observed in the steady field  $\mathbf{u}_\Delta$  and the  $f_1$ -frequency mode  $\boldsymbol{\varphi}_{f_1}$ , characterized by a dynamical system linearized around the steady-state field, also hold in transient processes.

Focusing on the temporal variation of each term, the diffusion term decreases monotonically over time for all  $Re$ , suggesting that diffusion effects become increasingly dominant as the  $f_1$ -frequency component evolves. Similarly,  $\mathcal{T}_{f_1 \rightleftharpoons f_1}|a_{f_1}|^2$  remains slightly negative. As seen in the time variation of  $N_{f_1}$  in figure 21 (also shown as the brown line in figure 22), all terms exhibit monotonic behavior at  $Re = 50$ . At  $Re = 60$ ,  $\mathcal{T}_{f_1 \rightleftharpoons f_1}|a_{f_1}|^2$  reaches a maximum before slightly decreasing to a steady state. Since this trend is absent in  $N_{f_1}$  at  $Re = 60$ , this suggests that  $Re = 60$  is close to the transition point where the monotonic development observed at  $Re = 50$  shifts to the nonlinear development seen at  $Re = 75$ . For  $Re = 75$  and 100, the decline after the peak of  $\mathcal{T}_{\Delta \rightarrow f_1}|a_{f_1}|^2$  becomes more pronounced. Notably, the peak of  $\mathcal{T}_{\Delta \rightarrow f_1}|a_{f_1}|^2$  nearly coincides with the minimum of  $N_{f_1}$ . This suggests that as energy transfer from the steady field to the  $f_1$ -frequency component increases, energy transfer to higher-frequency components also intensifies. That is, a hierarchical energy transfer structure can be inferred, where energy flows from the steady field into the  $f_1$ -frequency component and subsequently cascades from the  $f_1$ -frequency component to  $f_1$ -harmonics components.

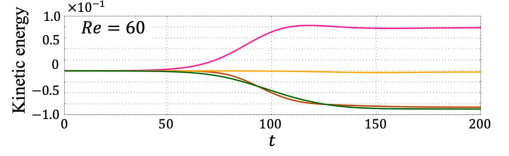
From the preceding discussion, it is evident that the primary energy supply responsible for the amplification of the  $f_1$ -frequency component is provided by the transfer term  $\mathcal{T}_{\Delta \rightarrow f_1}|a_{f_1}|^2$ . This motivates us to investigate the energy transfer fields  $\mathcal{T}_{\Delta \rightarrow f_1}|a_{f_1}|^2$ . Figure 23 shows the time-variation of energy transfer fields  $\mathcal{T}_{\Delta \rightarrow f_1}|a_{f_1}|^2$  at  $Re = 50, 60$ , and 100. The 0-line of  $\mathbf{u}_\Delta$  at the same  $t$  is plotted by the white line. The positive energy transfer region moves to the cylinders with time variation. At  $t = 80$  with a  $Re = 100$ , particularly strong energy transfer is observed near the recirculation region of the cylinder wake and on the  $y = 0$ . This distribution of energy transfer fields is very similar to transfer fields at post-transient flow fields at  $Re = 100$  reported in (Yeung *et al.* 2024). The distributions at  $t = 100$  and  $t = 30$  for  $Re = 100$  are quite different, but we can see how they gradually change continuously with time evolution. Continuous changes can be seen even at  $Re = 50$  and 60.

We focus on the relationship between the location of the recirculation region indicated by the white line and the energy transfer distribution. At  $Re = 100$ , the 0-line and energy transfer distributions maintain almost the same  $x$  position at all times. Conversely, for  $t = 300$  at

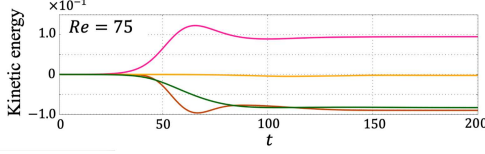
(a)



(b)



(c)



(d)

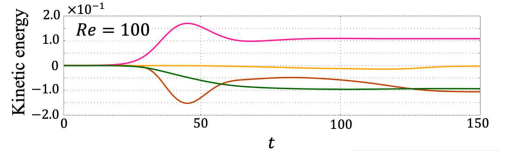
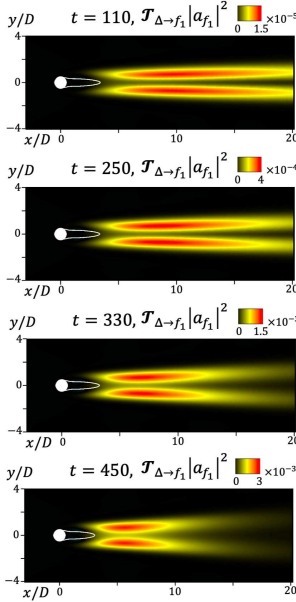
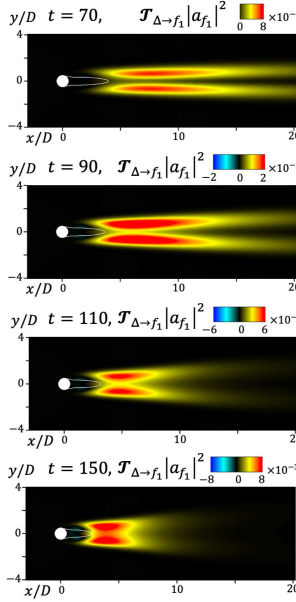


Figure 22: Time variation of four energy transfer term  $\mathcal{D}_{f_1} |a_{f_1}|^2$ ,  $\mathcal{T}_{\Delta \rightarrow f_1} |a_{f_1}|^2$ ,  $\mathcal{T}_{f_1 \rightleftharpoons f_1} |a_{f_1}|^2$ , and  $10N_{f_1}$ : (a)  $Re = 50$ , (b)  $60$ , (c)  $75$ , and (d)  $100$ .

(a)



(b)



(c)

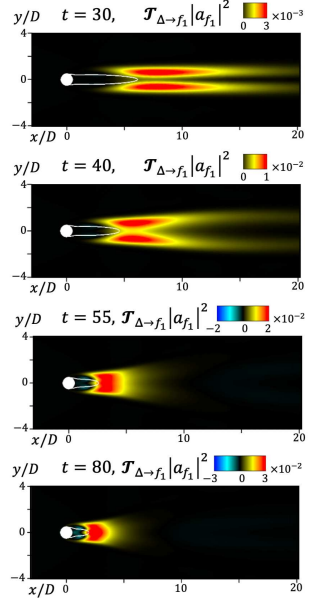


Figure 23: Spatial distribution of transfer fields  $\mathcal{T}_{\Delta \rightarrow f_1} |a_{f_1}|^2$  obtained from eigenmodes of tDMDpc (a)  $Re = 50$ , (b)  $60$ , and (c)  $100$ .

$Re = 60$  and  $Re = 50$ , the transfer distribution exists at a distance from the 0 line. It is possible that the difference in the development process between  $Re = 50$  and  $100$  (see figure 21) is due to this difference in the transfer fields. Even under conditions that eventually lead to a periodic flow, the system undergoes different transient processes. Energy transfer and budget analysis during the transient process is effective for investigating the underlying dynamics.

## 6. Conclusion

This paper presents an energy transfer and budget analysis method for flow fields with growing or decaying modes. Furthermore, our approach extends to nonlinear development

scenarios. The energy transfer analysis is achieved using a projection-based ROM for operator eigenmodes obtained from GSA and DMD. The projected governing equations are organized using the bi-orthogonality between the eigenmodes of the operators and their adjoint modes. The equation is further simplified by considering the interaction of frequencies in a triadic relationship based on the frequencies of the operator eigenmodes. Based on the simplified equations, we derived the global energy transfer equations for the entire flow field at the frequencies of interest. The global energy transfer equations were developed into a simplified form when the equation is linearized around a steady field and into an advanced form when accounting for the time-varying operators and modes.

The transfer analysis results using GSA eigenmodes around a steady flow show that the growth rate obtained from GSA is expressed by the sum of energy transfer from the steady flow to the eigenmode, self-decay derived from the convection of the eigenmodes, and viscous diffusion. This indicates that the growth or decay of eigenmodes is governed by their energy budget. For the flow around a cylinder, the only source of eigenmode energy is the steady flow, and this supply is nearly nonexistent for  $Re$  values smaller than the bifurcation point. The decrease in the growth rate at  $Re$  lower than the bifurcation point is caused by the self-decay from the convection of the eigenmode. The spatial distributions causing these transfers and diffusion were computed from the eigenmodes and the steady field inspired by other modal energy analysis methods.

The energy transfer and budget analysis were extended to the transient development process by considering the time variation of eigenmodes due to time-varying operators. To extract time-varying operator eigenmodes, we introduced tDMDpc, which regulates the initial phase and applies DMD to data obtained from multiple numerical simulation cases. Using tDMDpc for two-dimensional flow around a cylinder, we obtained time-varying eigenmodes that grow from a steady field to a periodic unsteady scenario. The base flow is obtained by averaging the numerical results across different initial conditions. For flow around a cylinder, the recirculation region of the wake becomes smaller as the unstable eigenmode grows.

Using the time-varying eigenmodes obtained by tDMDpc, we computed the energy budget for the global energy transfer equation. This analysis specifically applies to the operator's time-varying eigenmodes rather than being restricted to modes from tDMDpc extraction. In the flow around a cylinder, energy transfer from the base flow to the lowest-frequency eigenmode drives transient development. Simultaneously, nonlinear interactions induce an energy cascade into higher-frequency modes, which peaks alongside the energy transfer to the lowest-frequency eigenmode. The spatial distribution of transfer fields in the transient process indicates that a substantial amount of energy transfer from the base flow is concentrated around the recirculation region. Since this energy transfer field varies throughout the transient process, it serves as a powerful tool for observing the time-varying energy transfer distribution and discovering new flow physics.

## Appendix A. Grid convergence

The computational grid used in this study is validated based on the parameter dependence check. Regular grids and fine-long grids were prepared to test the effect on numerical results of the grid width and the far-field boundary size. Figure 24 shows the grid widths of the grids located on the  $x$ -axis in the two computational grids. The regular and fine-long grids accelerate the expansion of the grid width when the radius is greater than 55 and 147, respectively. The expansion ratio of the neighboring cell is less than or equal to 1.1. The number of cells for fine-long grids is 580 in the wall-parallel direction and 2260 in the wall-normal direction.

Numerical simulations were performed for a  $Re = 150$  using two computational grids.

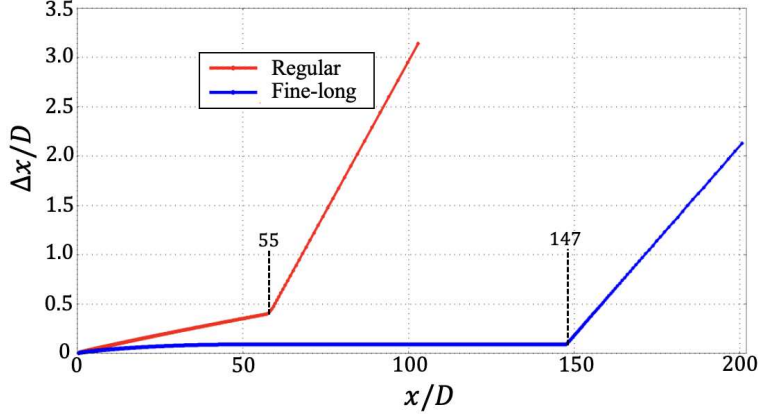


Figure 24: Cell width for regular and fine-long grid.

CFL number is set at less than or equal to 1.0 based on the validation of our previous work (Nakamura *et al.* 2024b). For quantitative comparison, the time-averaged velocity field  $\bar{\mathbf{u}}(\mathbf{x})$  and the time-averaged kinetic energy  $\overline{\tilde{u}\tilde{u}}(\mathbf{x})$  and  $\overline{\tilde{v}\tilde{v}}(\mathbf{x})$  are computed as

$$\bar{\mathbf{u}}(\mathbf{x}) = \frac{1}{T} \int \mathbf{u}(t, \mathbf{x}) dt, \quad (\text{A } 1)$$

$$\overline{\tilde{u}\tilde{u}}(\mathbf{x}) = \frac{1}{T} \int \tilde{u}(t, \mathbf{x}) \tilde{u}(t, \mathbf{x}) dt = \frac{1}{T} \int u(t, \mathbf{x}) u(t, \mathbf{x}) dt - \bar{\mathbf{u}}(\mathbf{x}) \bar{\mathbf{u}}(\mathbf{x}), \quad (\text{A } 2)$$

$$\overline{\tilde{v}\tilde{v}}(\mathbf{x}) = \frac{1}{T} \int \tilde{v}(t, \mathbf{x}) \tilde{v}(t, \mathbf{x}) dt = \frac{1}{T} \int v(t, \mathbf{x}) v(t, \mathbf{x}) dt - \bar{\mathbf{v}}(\mathbf{x}) \bar{\mathbf{v}}(\mathbf{x}), \quad (\text{A } 3)$$

based on Asada (2014). Here,  $T$  is set to 300, which is long enough since the primary dimensionless period of the vortex shedding is about 5.

Figure 25 shows the distribution of  $\bar{\mathbf{u}}(\mathbf{x})$ ,  $\overline{\tilde{u}\tilde{u}}$ , and  $\overline{\tilde{v}\tilde{v}}$  in the  $x$  and  $y$  directions. The distributions in the  $x$  direction for  $x/D < 20$  shown in figure 25 (a) are in better agreement for the regular and fine-long grids. The range of the  $x$ -direction was chosen because most of the energy transfer occurs at  $x/D < 20$ . Since the deviation of the kinetic energy distribution is relatively larger than that of the average field, the kinetic energy distribution is focused in the  $y$  direction distribution shown in figure 25 (b). The  $x$ -section coordinates position was chosen to be  $x/D = 2.23$  and 20.  $x/D = 2.23$  is selected since the peak value position of  $\overline{\tilde{v}\tilde{v}}$  on the  $x$ -axis. The  $y$ -axis distribution of kinetic energy in the streamwise direction at  $x/D = 2.23$  and 20 is in close agreement with the regular and fine-long grids. Therefore, the resolution of numerical results with the regular grid is enough for this work.

## Appendix B. Validation of time stepping GSA and parameter dependance

We check the validity of time-stepping GSA and the resulting eigenvalues and eigenmodes. The validity is divided into two parts: checking the dependance of parameters in time-stepping GSA and checking  $Re$  dependance.

### B.1. Time-stepping GSA parameter dependance

Time-stepping GSA has two parameters,  $\Delta T$  and  $\epsilon_0$ . In this paper,  $\Delta T$  is fixed at 0.1, and the parameter dependance is tested by varying the magnitude of  $\epsilon_0$ .

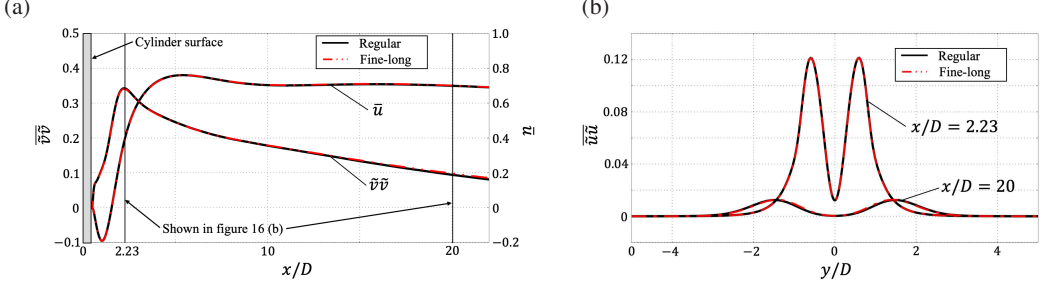


Figure 25: Comparison of the regular grid and fine-long grid with the average value of kinetic energy distribution  $\bar{u}u$ ,  $\bar{v}v$ , and streamwise velocity fields  $\bar{u}$ : (a) distribution on the x-axis of  $\bar{v}v$  and  $\bar{u}$ , (b) y-direction distribution of  $\bar{u}u$  and  $\bar{u}$  at  $x/D = 20$ , 2.23.  $x/D = 2.23$  is the peak value position of  $\bar{v}v$ .

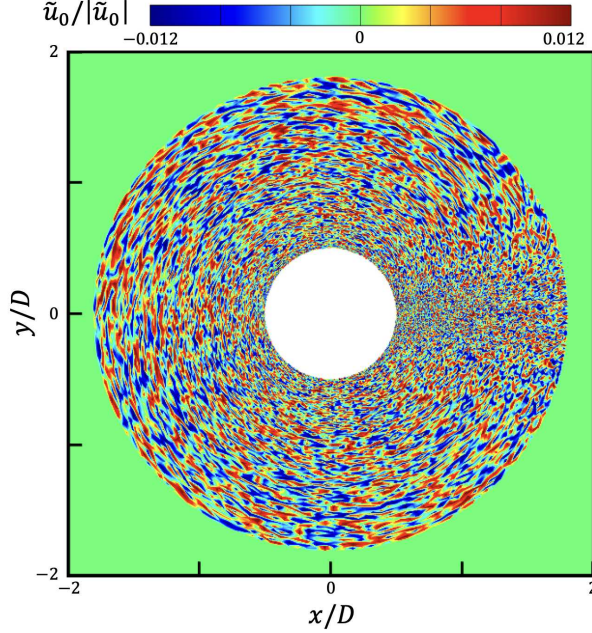


Figure 26: Initial disturbance for streamwise-velocity component at time-stepping GSA.

For investigate the effect of  $\epsilon_0$ , time-stepping GSA was performed on  $\epsilon_0 = 10^{-6}, 10^{-3}$ , and  $10^0$  at  $Re = 100$ . Figure 26 shows the initial disturbance at  $\epsilon_0 = 10^{-3}$ . Following Ranjan *et al.* (2020), the initial disturbance was generated only near the cylinder. Figure 27 shows instantaneous streamwise components of velocity and perturbation. For  $\epsilon_0 = 10^{-6}$  and  $10^{-3}$ , the distribution of streamwise component is an almost steady field. This is because the amount of perturbation, whose absolute value is determined by  $\epsilon_0$ , is smaller than that of the steady field. In contrast, when  $\epsilon_0 = 10^0$ , the magnitude of the perturbation is larger than the magnitude of the steady field, and the flow distribution is unphysical. In addition, for small values of  $\epsilon_0 = 10^{-6}$ , the perturbation distribution is symmetric to  $y = 0$ , and no asymmetric Karman vortex is formed. This is due to the suppression of fluctuations by small  $\epsilon_0$  during the development process of disturbance, and disturbance does not grow to the formulation of the Karman vortex.



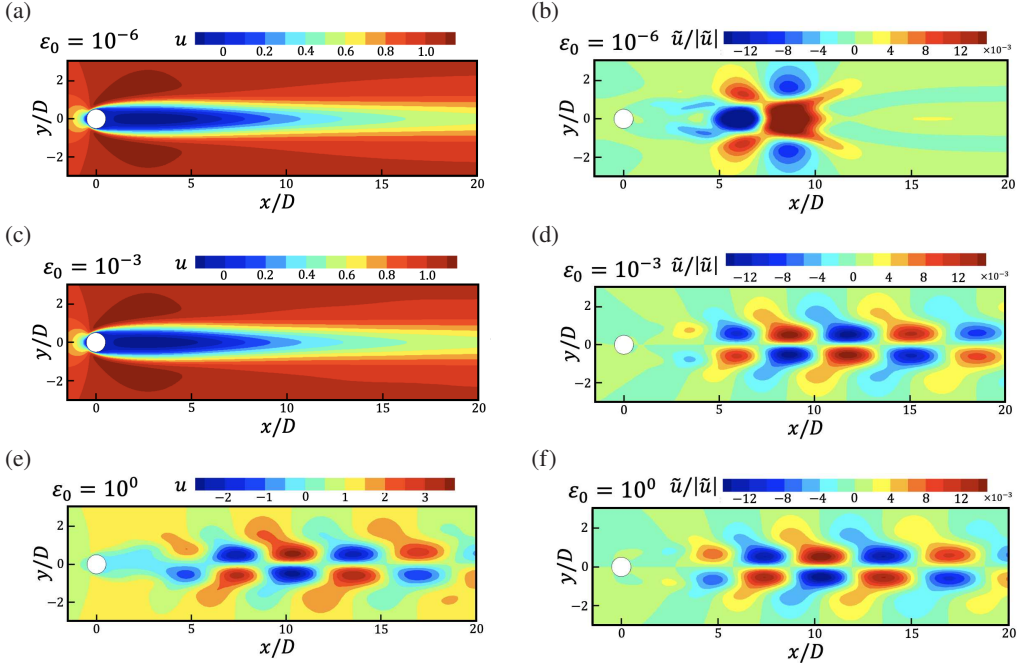


Figure 27: Instantaneous streamwise component of velocity and perturbation at  $Re = 100$  and  $t = 50$  in the time-stepping approach: (a) velocity with ( $\epsilon_0 = 10^{-6}$ ), (b) perturbation with ( $\epsilon_0 = 10^{-6}$ ), (c) velocity with ( $\epsilon_0 = 10^{-3}$ ), (d) perturbation with ( $\epsilon_0 = 10^{-3}$ ), (e) velocity with ( $\epsilon_0 = 10^0$ ), and (f) perturbation with ( $\epsilon_0 = 10^0$ ).

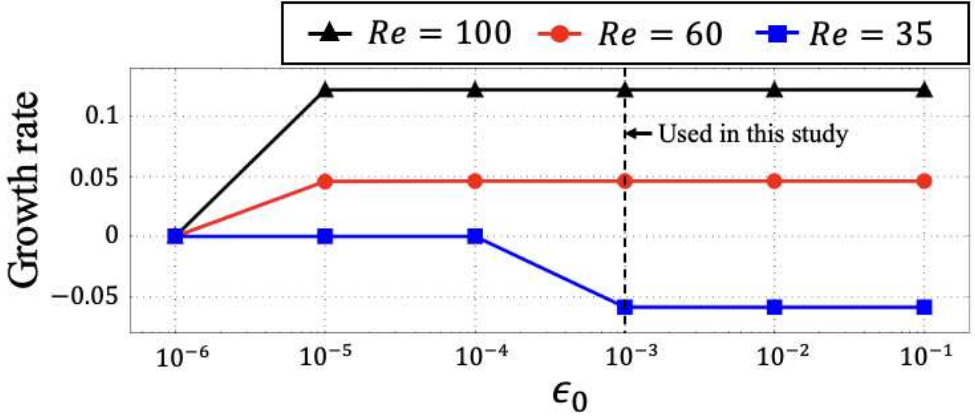


Figure 28: Variation of growth rate for various  $\epsilon_0$  with  $Re = 35, 60, 100$ .

To quantitatively evaluate the effect of  $\epsilon_0$ , growth rates were computed for several  $\epsilon_0$  and  $Re$  cases. Figure 28 shows the variation of growth rate with respect to  $\epsilon_0$  at  $Re = 35, 60$ , and  $100$ . The growth rate is constant for all  $Re$  cases when  $\epsilon_0$  is sufficiently large. However, in general, time-stepping GSA must be performed within a range where  $\epsilon_0$  is small; otherwise, the flow fields grow beyond the linear growth region. Therefore, this study uses  $\epsilon_0 = 10^{-3}$  in all cases.



---

$Re$	Growth rate	Frequency
45.0	$-7.79034 \times 10^{-3}$	0.115833
46.5	$-1.37338 \times 10^{-3}$	0.116221
46.6	$-9.54785 \times 10^{-4}$	0.116246
46.7	$-5.37557 \times 10^{-4}$	0.116269
46.8	$-1.21642 \times 10^{-4}$	0.116294
46.9	$2.93599 \times 10^{-4}$	0.116319
47.0	$7.07521 \times 10^{-4}$	0.116343
50.0	$1.26154 \times 10^{-2}$	0.116973

---

Table 1: Growth rate and frequency near the bifurcation point.

---

### B.2. Validation for Reynolds number dependance

Since the comparison with previous studies on the Reynolds number dependance is mentioned in figure 7, here we compare our results with those of ordinary CFD results. However, due to the difficulty of comparing the results of CFD and GSA under conditions of rapidly developing conditions at a relatively high  $Re$ , the results are compared near the bifurcation point. The growth rates and frequencies near the bifurcation point are shown in table 1. Between  $Re = 46.8$  and  $46.9$ , the growth rate changes from negative to positive. Since the absolute value of the growth rate is minimum at  $Re = 46.8$ , the bifurcation point is roughly 46.8.

The development of flow fields with  $Re = 46.8$  and  $46.9$  are computed by CFD without explicitly including disturbances. Figure 29 shows the residuals of the velocity vector in the flow field obtained by CFD. Here, the velocity residual is computed by

$$(\text{Velocity residual}) = \frac{1}{N\Delta T} \sum_{i=1}^N |\mathbf{u}(\mathbf{x}_i, t + \Delta T) - \mathbf{u}(\mathbf{x}_i, t)|, \quad (\text{B } 1)$$

where  $\mathbf{x}_i$  represents  $i$ th grid points. No increase in residuals is confirmed for  $Re = 46.8$ , but for  $Re = 46.9$ , the residuals gradually increase. An increase in residuals implies a sign of non-stationarity. Hence, the bifurcation point in the CFD obtained by the GSA is in close agreement. To compare the frequency of growing modes from CFD, DMD is applied to  $t = 1000$ – $2000$  at  $Re = 46.9$ . The obtained frequency is 0.116305, and growth rate is  $4.87011 \times 10^{-4}$ . Therefore, the time-stepping GSA presents the linear growing eigenmodes in the CFD.

## Appendix C. Convergence study of tDMDpc

For tDMDpc,  $j_{\max}$  is the number of snapshots in the eigenmode extraction using DMD. The validity of eigenmode extraction for time-dependent operators can be evaluated by the fact that the eigenmodes remain constant when the number of snapshots is sufficiently large. First, we check that the average field over  $\alpha$  does not change as increasing  $j_{\max}$ .

Figure 30 shows the time variation of the average field over  $\alpha$  at  $y/D = 0$  for  $j_{\max} = 20$  and 100. The average fields during the development process are completely consistent between 20 and 100 cases, and the average field for  $j_{\max} = 20$  cases is well converged. To quantitatively evaluate whether the flow field reaches a periodic state after the transient development, the mean field of the fully developed periodic flow is shown by the blue dotted line. Note that the fully developed periodic flow refers to the flow fields at  $t \geq 2000$ , averaged over  $t = 2000$ –

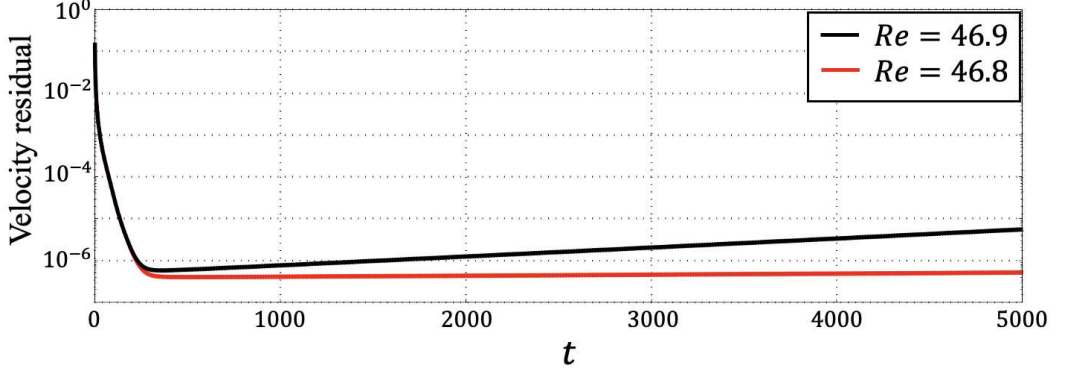


Figure 29: Velocity residuals for the numerical simulation at  $Re = 46.8$  and  $46.9$ . In the present simulation, critical  $Re$  is determined to be  $46.8$ , as the velocity residual remains at a constant order, which is consistent with the GSA result.

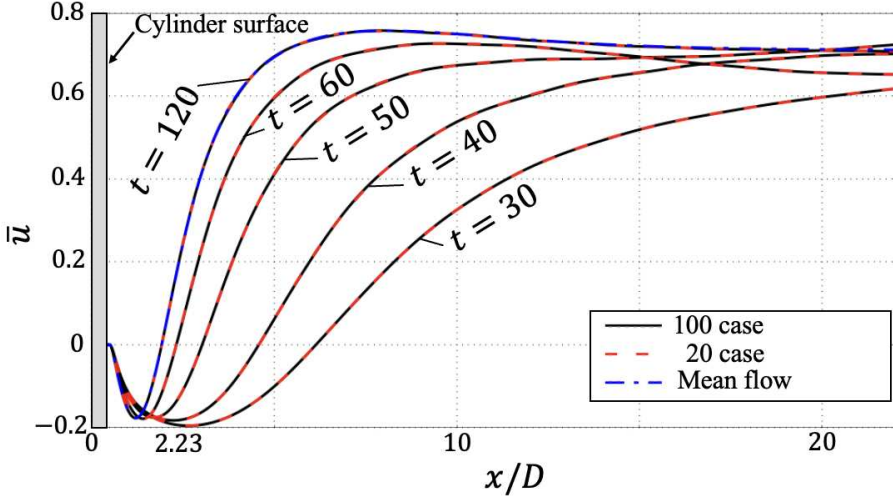


Figure 30: Average-fields of phase-controlled transient flow at  $Re = 100$ . Flow fields are averaged over 20 and 100 cases at  $t = 30, 40, 50, 60, 80$ , and  $120$ . The blue dash-dot line shows the mean fields of the post-transient flow field, which is obtained from time-averaging of fully developed periodic flow fields.

2300, and not averaged over  $\alpha$ . Moreover, after a sufficient time evolution, the average field over  $\alpha$  exhibits a reasonable distribution, as it coincides with the mean-field represented by the blue dotted line.

We check the convergence of the eigenmodes of the non-0 frequencies of the time-varying operator. Turning to the mode extraction process in the DMD, the eigenmodes are computed by projecting the eigenmodes of the low-dimensional operator  $\tilde{A}$  by  $U_r^T$ . Since  $U_r$  is determined by the SVD of the dataset, the convergence of the matrix projected by  $U_r$  is confirmed by the singular values. Then, in a form independent of the number of snapshots, we define

$$\gamma_k = \frac{\sigma_k^2}{(M-1)} \quad (\text{C } 1)$$

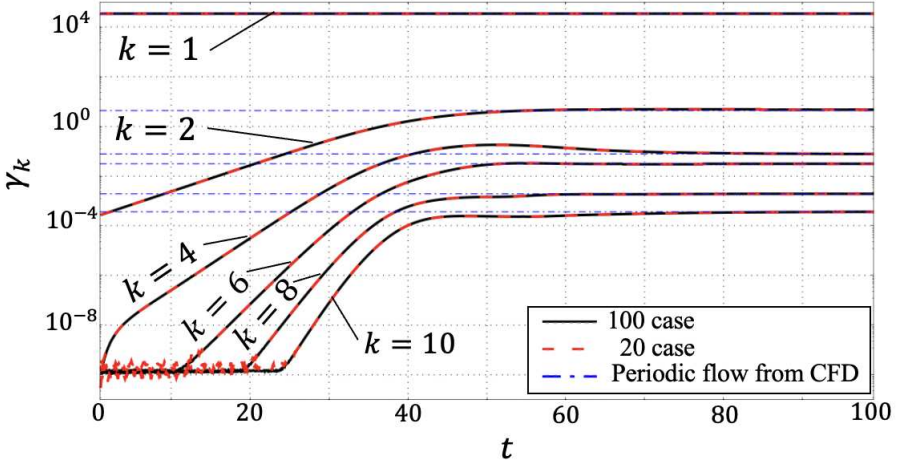


Figure 31: Square quantities of the singular value obtained from the SVD for matrix  $X$  in the DMD algorithm. All singular values were normalized by snapshot number, indicated in (C1). The blue dash-dot line is the  $\gamma_k$  computed from fully developed periodic flow fields.

where  $\sigma_k$  is the singular value of matrix  $X$ , thus,  $k$ th diagonal elements of  $S_r$  in equation (2.11), and  $M$  is the number of snapshots in the dataset. Here,  $\gamma_k$  equals the eigenvalue of variance-covariance matrix  $XX^T/\sqrt{M-1}$  and POD eigenvalue. The convergence of  $\gamma_k$  with respect to snapshot number means the convergence of the major features of the snapshots that make up the matrix  $X$  and ensures a sufficient number of snapshots. This also suggests the DMD modes computed using the SVD results for  $X$  converge.

Figure 31 shows the time variation of  $\gamma_k$  for  $j_{\max} = 20$  and 100 cases. The  $\gamma_k$  of DMD applied to the fully developed periodic flow is shown by the blue dotted line. Since singular values appear in pairs— $k = 2$  and 3,  $k = 4$  and 5,  $\dots$ —the one with the larger is plotted in the figure.  $k = 1$  corresponds to a mean field with no pair  $\gamma_k$  and, as shown in figure 30, has the same value at  $j_{\max} = 20$  and 100. The time variation of the value of  $\gamma_1$  appears to be almost negligible because the energy of the main flow is very large with respect to the transient variation for the cylinder backward.  $k = 2$  corresponds to the most dominant eigenmode and is well converged at all times. For  $k \geq 4$ , in the early stage of development,  $\gamma_k$  value is very small and is considered to be affected by the errors in the numerical calculation of SVD. In the early stage, the spatial structure corresponding to  $k \geq 4$  is too small or does not exist because the mode corresponding to  $k \geq 4$  is not added to the disturbance at  $t = 0$ . However, after sufficient development,  $j_{\max} = 20$  and 100 are close agreement. Therefore,  $j_{\max} = 20$  is large enough for capturing the eigenmode of the time-varying operator.

**Acknowledgements.** We thank Prof. Oliver T. Schmidt for pointing to the convective instability. We gratefully acknowledge Dr. Yasuhito Okano for providing valuable knowledge about GSA. We thank Yuta Iwatani for the valuable discussions on nonlinear interactions and resolvent analysis and for pointing out the bi-orthogonality of the DMD mode.

**Funding.** The numerical simulations were performed on the supercomputer systems “AFI-NITY” and “AFI-NITY II” at the Advanced Fluid Information Research Center, Institute of Fluid Science, Tohoku University, and JAXA Supercomputer System Generation 3 (JSS3). This study was partially supported by a Sasakawa Scientific Research Grant from the Japan Science Society. This study was partially supported by JST SPRING, Grant Number JPMJSP2114, Japan.

**Declaration of interests.** The authors report no conflict of interest.

**Author ORCIDs.**

Y. Nakamura, <https://orcid.org/0009-0008-4118-1078>;  
 Y. Kuroda, <https://orcid.org/0009-0002-4578-5887>;  
 S. Sato, <https://orcid.org/0000-0002-9979-0051>;  
 N. Ohnishi, <https://orcid.org/0000-0001-5895-0381>

## REFERENCES

- AITZHAN, A., NOURI, A. G., GIVI, P. & BABAEI, H. 2025 Reduced order modeling of turbulent reacting flows on low-rank matrix manifolds. *Journal of Computational Physics* **521**, 113549.
- AKHTAR, I. 2008 Parallel simulation, reduced-order modeling, and feedback control of vortex shedding using fluidic actuators. PhD thesis, Virginia Polytechnic Institute and State University.
- AMIRI-MARGAVI, A. & BABAEI, H. 2024 Time-dependent low-rank input–output operator for forced linearized dynamics with unsteady base flows. *Journal of Fluid Mechanics* **1001**, A22.
- ASADA, K. 2014 Computational analysis of flow fields induced by a DBD plasma actuator toward separated-flow control. Master's thesis, University of Tokyo.
- BALLOUZ, E., DAWSON, S. T. M. & BAE, H. J. 2024 Transient growth of wavelet-based resolvent modes in the buffer layer of wall-bounded turbulence. In *Journal of Physics: Conference Series*, vol. 2753, p. 012002. IOP Publishing.
- BARKLEY, D. 2006 Linear analysis of the cylinder wake mean flow. *Europhysics Letters* **75** (5), 750.
- BERKOOZ, G., HOLMES, P. & LUMLEY, J. L. 1993 The proper orthogonal decomposition in the analysis of turbulent flows. *Annual review of fluid mechanics* **25** (1), 539–575.
- BISWAS, N. & BUXTON, O. R. H. 2024 Energy exchanges between coherent modes in the near wake of a wind turbine model at different tip speed ratios. *Journal of Fluid Mechanics* **996**, A8.
- DENG, N., NOACK, B. R., MORZYŃSKI, M. & PASTUR, L. R. 2019 Low-order model for successive bifurcations of the fluidic pinball. *Journal of Fluid Mechanics* **884**, A8.
- FORNBERG, B. 1980 A numerical study of steady viscous flow past a circular cylinder. *Journal of Fluid Mechanics* **98** (4), 819–855.
- FREEMAN, B. R. S., MARTINUZZI, R. J. & HEMMATI, A. 2023 Exploring the influence of span-wise boundary conditions on the wake of a thin flat plate using Fourier-averaged Navier–Stokes equations. *International Journal of Heat and Fluid Flow* **103**, 109176.
- FREEMAN, B. R. S., MARTINUZZI, R. J. & HEMMATI, A. 2024 Momentum analysis of complex time-periodic flows. *Journal of Fluid Mechanics* **979**, A50.
- FUKAMI, K. 2024 *Data-Driven Modeling and Control of Extreme Aerodynamic Flows: Super Resolution, Manifold Identification, and Phase-Amplitude Reduction*. University of California, Los Angeles.
- GIANNETTI, F. & LUCHINI, P. 2007 Structural sensitivity of the first instability of the cylinder wake. *Journal of Fluid Mechanics* **581**, 167–197.
- GOUPILLAUD, P., GROSSMANN, A. & MORLET, J. 1984 Cycle-octave and related transforms in seismic signal analysis. *Geoexploration* **23** (1), 85–102.
- GUAN, W., DONG, L., ZHANG, A. & CAI, Y. 2024 Output-only modal identification with recursive dynamic mode decomposition for time-varying systems. *Measurement* **224**, 113852.
- HERRMANN, B., BADDOO, P. J., SEMAAN, R., BRUNTON, S. L. & McKEON, B. J. 2021 Data-driven resolvent analysis. *Journal of Fluid Mechanics* **918**, A10.
- HOLMES, P. 2012 *Turbulence, coherent structures, dynamical systems and symmetry*. Cambridge university press.
- IWATANI, Y., ASADA, H., YEH, C.-A., TAIRA, K. & KAWAI, S. 2023 Identifying the self-sustaining mechanisms of transonic airfoil buffet with resolvent analysis. *AIAA Journal* **61** (6), 2400–2411.
- JIANG, H. & CHENG, L. 2017 Strouhal–Reynolds number relationship for flow past a circular cylinder. *Journal of Fluid Mechanics* **832**, 170–188.
- JIANG, H. & CHENG, L. 2019 Transition to the secondary vortex street in the wake of a circular cylinder. *Journal of Fluid Mechanics* **867**, 691–722.
- KAJISHIMA, T. & TAIRA, K. 2017 *Computational Fluid Dynamics Incompressible Turbulent Flows*. Springer.
- KUMAR, B. & MITTAL, S. 2006 Prediction of the critical Reynolds number for flow past a circular cylinder. *Computer Methods in Applied Mechanics and Engineering* **195** (44–47), 6046–6058.
- KUNISCH, K. & VOLKWEIN, S. 2002 Galerkin proper orthogonal decomposition methods for a general equation in fluid dynamics. *SIAM Journal on Numerical analysis* **40** (2), 492–515.

- LE, H. & MOIN, P. 1991 An improvement of fractional step methods for the incompressible Navier-Stokes equations. *Journal of Computational Physics* **92** (2), 369–379.
- LEONARD, B. P. 1979 A stable and accurate convective modelling procedure based on quadratic upstream interpolation. *Computer Methods in Applied Mechanics and Engineering* **19** (1), 59–98.
- LUCHINI, P. & BOTTARO, A. 2014 Adjoint equations in stability analysis. *Annual Review of Fluid Mechanics* **46** (1), 493–517.
- LUMLEY, J. L. 1967 The structure of inhomogeneous turbulent flows. *Atmospheric Turbulence and Radio Wave Propagation* pp. 166–178.
- MA, X. & KARNIADAKIS, G. E. 2002 A low-dimensional model for simulating three-dimensional cylinder flow. *Journal of Fluid Mechanics* **458**, 181–190.
- MITTAL, SANJAY 2009 Stability of flow past a cylinder: Energy budget of eigenmodes. *International Journal for Numerical Methods in Fluids* **63** (5), 533–547.
- MORLET, J., ARENS, G., FOURGEAU, E. & GLARD, D. 1982 Wave propagation and sampling theory—Part I: Complex signal and scattering in multilayered media. *Geophysics* **47** (2), 203–221.
- NAKAMURA, Y., SATO, S. & OHNISHI, N. 2024a Application of proper orthogonal decomposition to flow fields around various geometries and reduced-order modeling. *Computer Methods in Applied Mechanics and Engineering* **432**, 117340.
- NAKAMURA, Y., SATO, S. & OHNISHI, N. 2024b Reduced-order modeling for pressure field via global proper orthogonal decomposition. Proceedings of Twelfth international conference on computational fluid dynamics, Kobe, Japan.
- NAKAMURA, Y., SATO, S. & OHNISHI, N. 2025a Simulation method for finding a fixed point of Navier-Stokes equations by symmetricity constraints. *Under Review*.
- NAKAMURA, Y., SATO, S. & OHNISHI, N. 2025b Uncovering triadic interaction relationships latent in mode A behind a circular cylinder. *arXiv preprint arXiv:2504.00896*.
- NEKKANTI, A., PICKERING, E., SCHMIDT, O. T. & COLONIUS, T. 2025 Bispectral decomposition and energy transfer in a turbulent jet. *arXiv preprint arXiv:2502.15091*.
- NOACK, B. R., AFANASIEV, K., MORZYŃSKI, M., TADMOR, G. & THIELE, F. 2003 A hierarchy of low-dimensional models for the transient and post-transient cylinder wake. *Journal of Fluid Mechanics* **497**, 335–363.
- NOACK, B. R. & ECKELMANN, H. 1994a A global stability analysis of the steady and periodic cylinder wake. *Journal of Fluid Mechanics* **270**, 297–330.
- NOACK, B. R. & ECKELMANN, H. 1994b A low-dimensional Galerkin method for the three-dimensional flow around a circular cylinder. *Physics of Fluids* **6** (1), 124–143.
- NOACK, B. R., PAPAS, P. & MONKEWITZ, P. A. 2005 The need for a pressure-term representation in empirical Galerkin models of incompressible shear flows. *Journal of Fluid Mechanics* **523**, 339–365.
- OHMICH, Y. 2014 Global linear stability analysis of compressible vortical flows. PhD thesis, Department of Advanced Energy, The University of Tokyo.
- OHMICH, Y. 2024 Variational mode decomposition-based nonstationary coherent structure analysis for spatiotemporal data. *Aerospace Science and Technology* **149**, 109162.
- OHMICH, Y. & YAMADA, K. 2021 Matrix-free triglobal adjoint stability analysis of compressible Navier-Stokes equations. *Journal of Computational Physics* **437**, 110332.
- RANJAN, R., UNNIKRISHNAN, S. & GAITONDE, D. 2020 A robust approach for stability analysis of complex flows using high-order Navier-Stokes solvers. *Journal of Computational Physics* **403**, 109076.
- RINOSHIKA, A. & RINOSHIKA, H. 2020 Application of multi-dimensional wavelet transform to fluid mechanics. *Theoretical and Applied Mechanics Letters* **10** (2), 98–115.
- ROLANDI, L. V., RIBEIRO, J. H. M., YEH, C.-A. & TAIRA, K. 2024 An invitation to resolvent analysis. *Theoretical and Computational Fluid Dynamics* **38** (5), 603–639.
- SAPSIS, T. P. & LERMUSIAUX, P. F. J. 2009 Dynamically orthogonal field equations for continuous stochastic dynamical systems. *Physica D: Nonlinear Phenomena* **238** (23–24), 2347–2360.
- SATO, S. & SCHMIDT, O. T. 2025 Parametric reduced-order modeling and mode sensitivity of actuated cylinder flow from a matrix manifold perspective. *arXiv preprint arXiv:2502.03754*.
- SCHMID, P. J. 2007 Nonmodal stability theory. *Annual Review of Fluid Mechanics* **39** (1), 129–162.
- SCHMID, P. J. 2010 Dynamic mode decomposition of numerical and experimental data. *Journal of Fluid Mechanics* **656**, 5–28.
- SCHMID, P. J. 2022 Dynamic mode decomposition and its variants. *Annual Review of Fluid Mechanics* **54** (1), 225–254.



- SCHMIDT, O. T. 2020 Bispectral mode decomposition of nonlinear flows. *Nonlinear Dynamics* **102** (4), 2479–2501.
- SCHMIDT, O. T. & COLONIUS, T. 2020 Guide to spectral proper orthogonal decomposition. *Aiaa journal* **58** (3), 1023–1033.
- SEN, S., MITTAL, S. & BISMAS, G. 2009 Steady separated flow past a circular cylinder at low Reynolds numbers. *Journal of Fluid Mechanics* **620**, 89–119.
- STANKIEWICZ, W., MORZYŃSKI, M., KOTECKI, K. & NOACK, B. R. 2017 On the need of mode interpolation for data-driven Galerkin models of a transient flow around a sphere. *Theoretical and Computational Fluid Dynamics* **31**, 111–126.
- TAIRA, K., BRUNTON, S. L., DAWSON, S. T., ROWLEY, C. W., COLONIUS, T., McKEON, B. J., SCHMIDT, O. T., GORDEYEV, S., THEOFILIS, V. & UKEILEY, L. S. 2017 Modal analysis of fluid flows: An overview. *AIAA Journal* **55** (12), 4013–4041.
- TAIRA, K., HEMATI, M. S., BRUNTON, S. L., SUN, Y., DURAISAMY, K., BAGHERI, S., DAWSON, S. T. & YEH, C.-A. 2020 Modal analysis of fluid flows: Applications and outlook. *AIAA Journal* **58** (3), 998–1022.
- TANEDA, S. 1959 Downstream development of the wakes behind cylinders. *Journal of the physical society of Japan* **14** (6), 843–848.
- TOWNE, A., SCHMIDT, O. T. & COLONIUS, T. 2018 Spectral proper orthogonal decomposition and its relationship to dynamic mode decomposition and resolvent analysis. *Journal of Fluid Mechanics* **847**, 821–867.
- TREFETHEN, L. N., TREFETHEN, A. E., REDDY, S. C. & DRISCOLL, T. A. 1993 Hydrodynamic stability without eigenvalues. *Science* **261** (5121), 578–584.
- TU, J. H. 2013 Dynamic mode decomposition: Theory and applications. PhD thesis, Princeton University.
- WILLIAMSON, C. H. K. 1996 Vortex dynamics in the cylinder wake. *Annual Review of Fluid Mechanics* **28** (1), 477–539.
- YAMADA, M. & OHKITANI, K. 1991 An identification of energy cascade in turbulence by orthonormal wavelet analysis. *Progress of Theoretical Physics* **86** (4), 799–815.
- YEUNG, B., CHU, T. & SCHMIDT, O. T. 2024 Revealing structure and symmetry of nonlinearity in natural and engineering flows. *arXiv preprint arXiv:2411.12057*.
- YEUNG, B. & SCHMIDT, O. T. 2025 Spectral dynamics of natural and forced supersonic twin-rectangular jet flow. *arXiv preprint arXiv:2501.10894*.
- ZHANG, H., ROWLEY, C. W., DEEM, E. A. & CATTAFESTA, L. N. 2019 Online dynamic mode decomposition for time-varying systems. *SIAM Journal on Applied Dynamical Systems* **18** (3), 1586–1609.
- ZHANG, W. & WEI, M. 2017 Model order reduction using DMD modes and adjoint DMD modes. In *8th AIAA Theoretical Fluid Mechanics Conference*, p. 3482.
- ZHONG, Y., AMIRI-MARGAVI, A., BABAEI, H. & TAIRA, K. 2025 Optimally time-dependent modes of vortex gust-airfoil interactions. *arXiv preprint arXiv:2501.02095*.